`

FORMATION AND FATE OF A COASTAL DENSE WATER MASS:

THE 2021 TEXAS WINTER STORMS

A Thesis

by

MARIA YSABEL DAVID WANG

Submitted to the Graduate and Professional School of
Texas A&M University
in partial fulfillment of the requirements for the degree of

MASTER OF SCIENCE

Chair of Committee,	Steven F. DiMarco
Committee Members,	Cory Spencer Jones
	James Kaihatu
Head of Department,	Shari Yvon-Lewis

August 2023

Major Subject: Oceanography

ABSTRACT

In February of 2021, a series of winter storms moved across the southern continental United States, resulting in extreme cold temperatures on land and in coastal waters. The Texas Automated Buoy System (TABS) network recorded a sea surface temperature minimum of 10.73°C and a surface density maximum of 1025.25kg/m^3 south of Galveston Bay shortly after the winter storms, unusual values when compared with TABS's decades-long measurements in the coastal northwestern Gulf of Mexico. Hydrographic profiles collected in April 2021 in the same region show the presence of an anomalous subductive tongue: a distinct water mass characterized by an isohaline of 36.2 and density range 25.2kg/m^3 – 25.8kg/m^3 moving seaward from the full water-column along the continental shelf and subducting beneath the mixed layer at depths ~30 – 60m. The signal of the tongue diminished by September 2021 after being incorporated into background values. We have shown via various analyses and quantification of observations from 1995-2023 that the 2021 hydrography deviates from climatological values due to the presence of the water mass, substantiating the density anomaly of the tongue. 2021 observations allow us to connect the April tongue with the February winter storms, revealing the spatiotemporal extent of the event. Numerical hindcast results show that atmospheric forcing, particularly cooling and vertical mixing due to winds that resulted in homogenous water-columns, resulted in the formation of a surface dense water mass in the northwestern Gulf of Mexico. Analyses in temperature-salinity space shows that after formation along the shelf in February, the water mass mixed diapycnally with ambient water as it moved offshore and sank down the water-column, reaching neutral buoyancy under the upper mixed layer by April.

ACKNOWLEDGEMENTS

Thank you to my committee chair, Dr. DiMarco, for his guidance, patience, and mentorship on this thesis and throughout my time at Texas A&M that has shaped me as both a person and a researcher. I would also like to thank my committee members, Dr. Jones and Dr. Kaihatu, from whom I've learned so much over the course of this research.

Thanks also go to my friends and colleagues at the Texas A&M Department of Oceanography and the Geochemical and Environmental Research Group who have made this research possible and have been a continued source of support and friendship in the last two years.

Thank you to my incredibly supportive parents, brother, friends, and family, and my loving and understanding partner, who have always encouraged and believed in me.

Finally, thank you to my Texas family Paige, Amanda, Raquel, and Donna who have made me feel so loved and at home.

CONTRIBUTORS AND FUNDING SOURCES

Contributors

This work was supervised by a thesis committee consisting of Professor Steven DiMarco and Professor Spencer Jones of the Department of Oceanography and Professor James Kaihatu of the Department of Civil and Environmental Engineering.

The data analyzed for Chapter 3 were provided by Professor DiMarco, Professor Xinping Hu of Texas A&M University – Corpus Christi, and Dr. Leticia Barbero of the National Oceanic and Atmospheric Administration Atlantic Oceanographic and Meteorological Laboratory (NOAA-AOML). The general circulation model depicted in Chapter 3 was conducted by Dr. Jaison Kurian of the Department of Oceanography in 2022.

All other work conducted for the thesis was completed by the student independently.

Funding Sources

Graduate study was supported by a graduate research assistantship through the NOAA Research Ocean Acidification Program (OAP), the Texas A&M University Department of Oceanography Ralph Rayburn ’69 Scholarship, and the Society for Underwater Technology in the U.S. (SUT-US) Student Scholarship.

Data and observations collected by the Texas Automated Buoy System are funded through a contract to the Geochemical and Environmental Research Group at Texas A&M University by the Texas General Land Office Oil Spill division (1994-2003) soon to be 2025. Data and observations for the Louisiana-Texas Shelf Oceanography Program project were funded through a contract to Texas A&M University by the Minerals Management Service – Department of the Interior (Award number 14-35-0001-30509). Data and observations from the

Research Experience for Undergraduates cruises are funded through the National Science Foundation (Award numbers: 1455851, 1849932). Data and observations from the Mechanisms Controlling Hypoxia were funded by the NOAA Center for Sponsored Coastal Ocean Research (Grant numbers NA03N0S4780039, NA06N0S4780198, NA09N0S4780208). Data and observations from the Ocean Acidification on a Crossroad: Enhanced Respiration, Upwelling, Increasing Atmospheric CO_2, and their interactions in the northwestern Gulf of Mexico project (Grant number NA19OAR0170354) and the first, third, and fourth Gulf of Mexico Ecosystems and Carbon Cycle Cruises are funded by the NOAA OAP.

NOMENCLATURE

TABS	Texas Automated Buoy System
TGLO	Texas General Land Office
SST	Sea surface temperature
SSS_P	Practical sea surface salinity
TXLA Shelf	Texas-Louisiana Shelf
NOAA	National Oceanic and Atmospheric Administration
OAP	Ocean Acidification Program
GOMECC	Gulf of Mexico Ecosystems and Carbon Cycle Project
XR	Ocean Acidification at a Crossroad Project
GL	GOMECC Galveston Line
SUW	Subtropical Underwater
LATEX	Louisiana-Texas Shelf Oceanography Program
MCH	Mechanisms Controlling Hypoxia
REU	Research Experience for Undergraduates
TS Space	Temperature-Salinity Space
PVD	Progressive Vector Diagram
GCM	General Circulation Model

TABLE OF CONTENTS

Page

ABSTRACT ii
ACKNOWLEDGEMENTS iii
CONTRIBUTORS AND FUNDING SOURCES iv
NOMENCLATURE vi
TABLE OF CONTENTS vii
LIST OF FIGURES viii
LIST OF TABLES xi
1. INTRODUCTION 1
1.1. Background 1
1.2. Gulf of Mexico hydrography 5
1.2.1. Hydrography and coastal water masses in the northwestern Gulf of Mexico 5
1.2.2. Deep water masses in the Gulf of Mexico 7
1.3. Dense water mass formation and cascading along continental shelves 8
1.3.1. Dense water mass formation due to cold-air outbreaks 8
1.3.2. Dense water mass cascading and export 9
1.4. Research questions 11
1.5. Scientific hypotheses 11
1.6. Thesis organization 12
2. DATA AND METHODS 13
2.1. Data 13
2.1.1. Observational data 15
2.1.2. Numerical data 16
2.2. Methods 17
2.2.1. Data analysis 17
2.2.2. Volumetric calculation of the water mass 17
2.2.3. Progressive vector diagram (PVD) 18
2.2.4. Numerical modeling of idealized diffusion 18
3. RESULTS AND DISCUSSION 20
3.1. GOMECC Galveston Line (GL) cross-sections 20
3.1.1. Multi-year seasonal GL cross-section comparison 20
3.1.2. Analysis in Temperature-Salinity (TS) space 28
3.1.3. Volumetric calculation of the dense water mass 31
3.1.4. Progressive vector diagrams (PVDs) 33
3.2. General circulation model (GCM) results 35

3.2.1. Comparison of GCM and nearshore TABS network timeseries 35
3.2.2. Generation of dense surface water in the GCM 36
3.3. Idealized diffusion model results 39
4. SUMMARY AND CONCLUSIONS 46
REFERENCES 49

LIST OF FIGURES

FIGURE Page

Fig. 1.1. 40-hour Lanczos low-pass-filtered hourly timeseries of wind speed, air temperature, sea surface temperature (SST), sea surface practical salinity (SSS_P), and calculated sea surface density minus 1000 (σ) at Buoy B of the TABS network in February 2021.....2

Fig. 1.2. Timeseries and 2021 anomaly plots of sea surface temperature (SST) (top) and sea surface practical salinity (SSS_P) (bottom) from Buoy B of the TABS network. For each hydrographic property, data from 2021 is in solid blue lines, and climatological data averaged over 1995-2020 is in orange lines. The anomaly of the 2021 data with respect to the climatology is shown under the timeseries plots and are calculated as $\Delta a_i = a_{i,2021} - a_{c,i}$ where $a_{i,2021}$ is the SST or SSS_P observation from Buoy B on day i in 2021 and $a_{c,i}$ is the buoy climatology for day i. The datasets are all averaged over each calendar day. The duration of the winter event (February 10-20, 2021) is indicated by the first shaded blue block, and the XR01 cruise date (April 23, 2021) is indicated by the second shaded blue block. 3

Fig. 1.3. Locations of TABS Buoy B (black square), Galveston (black triangle), Houston (black circle), XR01 stations (blue circles), and XR02 stations (orange diamonds) stations along the GL at 95°W. 4

Fig. 1.4. Temperature-Salinity diagram of GL profiles in April and August 2021: XR01 (blue circles) and XR02 (orange diamonds). 5

Fig. 1.5. Climatological sea surface temperature (SST), sea surface practical salinity (SSS_P), and wind speed timeseries averaged per calendar day over 16 years (1995-2020) of Buoy B. 6

Fig. 1.6. Histogram (bin width 0.5°C) of Buoy B sea surface temperature (SST) from 1995-2020.....7

Fig. 2.1. Locations of all observational stations used in this study classified by dataset (Table 2.1). 13

Fig. 3.1. Cross-sections of XR01 (April 2021) profiles along the GL of practical salinity (top), temperature (middle), and density minus 1000 (σ) (bottom). Black triangles are data collection latitudes: downward-facing triangles are located within the cross-section bounds and rotated triangles are outside of the bounds at 28.6°N and 27.33°N. The subductive tongue in the salinity cross-section (~36.2 in black) is seen subducting under the 22°C mixed layer. Converging isopycnals in the offshore density cross-section is highlighted. 24

Fig. 3.2. Cross-sections of XR02 profiles (August 2021) along the GL of practical salinity (top), temperature (middle), and density minus 1000 (σ) (bottom). Black triangles are data collection latitudes: downward-facing triangles are located within the cross-section bounds and rotated triangles are outside of the bounds at 28.68°N and 27.33°N. 25

Fig. 3.3. Cross-sections of XR05 (March 2023) profiles along the GL of practical salinity (top), temperature (middle), and density minus 1000 (σ) (bottom). Black triangles are data collection latitudes: downward-facing triangles are located within the cross-section bounds and the rotated triangle is outside of the bounds at 29°N. 26

Fig. 3.4. First-order difference (Δ) between the cross-sections of XR05 (Fig. 3.3) and XR01 (Fig. 3.1) along the GL of practical salinity (S_P) (top), temperature (T) (middle), and density minus 1000 (σ) (bottom). Black diamonds and red triangles are data collection latitudes of XR01 and XR05 respectively; solid shapes are located within the cross-section bounds and hollow shapes are outside the bounds (XR01: 28.6°N and 27.33°N, XR05: 29°N). 27

Fig. 3.5. Temperature-Salinity diagram of GL profiles in 2021: XR01 (blue circles), XR02 (orange diamonds), and GOMECC4 (dark blue squares). Red arrows and circles point out the salinity minima of each sharp curve. The density range in the cross-sections (Fig. 3.1 and Fig. 3.2) of 25.0kg/m^3 – 26.5kg/m^3 is highlighted. 29

Fig. 3.6. Temperature-Salinity diagram of climatology, XR cruises, and GOMECC4 cruise profiles along the GL profiles for the entire TS range (top) and zoomed into the area of mixing (bottom). Climatology is composed of data from Table 2.1. Red arrows and circles point out the sharp curves in XR01, XR02, and GOMECC4. The density range in the cross-sections (Fig. 3.1 and Fig. 3.2) of 25.0kg/m^3 – 26.5kg/m^3 is highlighted. 30

Fig. 3.7. Volumetric calculation of TS_P properties of the interpolated XR01 and XR02 transects (Fig. 3.1 and Fig. 3.2). 1 count unit corresponds to 111,000m^3. The intersection of the dashed red boxes is the hydrographic range of the XR01 curve that deviates from climatology in TS space (Fig 3.5 and Fig. 3.6). The density range of the water mass (25.2 kg/m^3 ≤ σ_{WM} ≤ 25.8kg/m^3) is highlighted. 32

Fig. 3.8. Histogram (bins of 0.2kg/m^3) of density minus 1000 σ along the GL during XR01 and XR02. 1 count corresponds to 111,000m^3. The water mass density range (25.2 kg/m^3 ≤ σ_{WM} ≤ 25.8kg/m^3) is contained within the dashed red box. 33

Fig. 3.9. Hourly Progressive vector diagrams (PVD) of SSS_P (left) and SST (right) of TABS Buoys B, D, and X from 10 (t_0) – 16 February (t_{end}) 2021. 34

Fig. 3.10. Timeseries of sea surface temperature (SST, top) and sea surface salinity (SSS, bottom) from the TABS Buoy B (solid blue line) and from the GCM (dashed orange line) from February-April 2021. The duration of the winter storms (10-20 February)

is within the shaded blue region where the Buoy B SSS_P increase occurs (red arrow). 35

Fig. 3.11. **Left:** Temperature-Salinity diagram of GCM results of five stations along the GL (inset). Triangular points represent hydrographic data at each station (indicated by the different colors in the inset) before the winter storm event (8 Feb 2021), and circular points represent hydrographic data at the same depths at each station under the influence of the event (16 Feb 2021). The points corresponding to each station are separated by 10 m, starting from the surface (i.e., 0 m). Following from Nowlin and Parker (1974), triangular points enclosed in black squares and circular points enclosed in black circles represent the surface mixed layer at each indicated station before and during the event, respectively. Arrows indicate the temporal evolution of the mixed layer hydrographic properties in TS space, pointing from the station properties before the event (e.g. 2) to during the event (e.g. 2'). The dashed line connects the hydrographic properties at the surface of all stations during the storm. **Right:** Reprinted and modified from Nowlin and Parker (1974) during a cold-air outbreak in January 1966. 38

Fig. 3.12. Smoothed practical salinity (top), temperature (middle), and density minus 1000 (σ) (bottom) of the idealized diffusion model at t_0 = 0 hours. Black triangles are XR05 data collection latitudes. The 26kg/m^3 isopycnals, i.e., the high-density water mass along the shelf and in the offshore deep ocean, are highlighted. 42

Fig. 3.13. Smoothed practical salinity (top), temperature (middle), and density minus 1000 (σ) (bottom) of the idealized diffusion model at t_{12} = 12 hours. Black triangles are XR05 data collection latitudes. The current timestep 26kg/m^3 isopycnals, and those for t_0 are also shown. 43

Fig. 3.14. Smoothed practical salinity (top), temperature (middle), and density minus 1000 (σ) (bottom) of the idealized diffusion model at t_{336} = 336 hours = 2 weeks. Black triangles are XR05 data collection latitudes. The current timestep 26kg/m^3 isopycnals, and those for t_0 and t_{12} are also shown. 44

Fig. 3.15. Differences (Δ) between the final (t_{336}, Fig. 3.14) and first (t_0, Fig. 3.12) timesteps of the idealized diffusion model of smoothed practical salinity (S_P) (top), temperature (T) (middle), and density minus 1000 (σ) (bottom). Black triangles are XR05 data collection latitudes. Text annotations (saltier, warmer, etc.) refer to conditions of t_{336} in comparison to those at t_0. 45

LIST OF TABLES

TABLE Page

Table 1.1. Coordinates of XR01 and XR02 stations along the GL.....4

Table 2.1. Datasets, respective projects, inclusive dates, and descriptions used in this study. 14

Table 3.1. Volumetric calculation of the dense water mass during XR01 and XR02. 33

Table 3.2. Temperature (T), practical salinity (S_P), and density (σ) ranges for the idealized diffusion model timesteps t_0, t_{12}, and t_{336}. The lower and upper bounds of these ranges are determined by the colorbar limits in Fig. 3.12 to Fig. 3.14. 39

1. INTRODUCTION

1.1. Background

In February 2021, a series of winter storms brought unprecedented cold temperatures to the southern continental United States, resulting in massive infrastructure failures in Texas and impacting millions (Doss-Gollin et al., 2021). Under the influence of the storms, the nearshore buoy B (Fig. 1.3) of the Texas Automated Buoy System (TABS), the regional observation network of the coastal northwestern Gulf of Mexico funded by the Texas General Land Office (TGLO) (Walpert et al., 2020), recorded an air temperature minimum of -8.64°C on 16 February 2021, a sea surface temperature (SST) minimum of 10.73°C on 21 February 2021, and a sea surface practical salinity (SSS_P) (Intergovernmental Oceanographic Commission, 2015; UNESCO, 1981) maximum of 33.2 on 18 February 2021 (Fig. 1.1) – these deviated greatly from typical values in comparison to the 25-year climatology of the TABS network (Fig. 1.2 and Fig. 1.6). SST and SSS_P during and after the storms resulted in a surface density of 1025.25 kg/m^3on 25 February 2021, an unusual value in this location.

Two research cruises were conducted in 2021 (April and August) under the *Ocean Acidification at a Crossroad* project funded by the NOAA Ocean Acidification Program (Table 2.1). Hydrographic profiles along a 95°W transect called the "GOMECC Galveston Line" (GL) (Fig. 1.3, Table 1.1) from the April 2021 cruise, the first Crossroad cruise henceforth referred to in this document as "XR01," showed a high-salinity tongue of dense water that extended from the coast surface past the shelf break to the subsurface. By the second Crossroad cruise in August 2021 cruise henceforth referred to as "XR02," the strength of the tongue had diminished.

The Texas-Louisiana shelf has been continuously monitored for more than three decades. These observations show that the temperature and practical salinity profiles recorded during XR01 (Fig. 1.4) were consistent with a relationship between the XR01 surface and deep tongue and the fate of the dense surface water mass that formed during the winter storms, and that the diminishing of the subductive tongue signal from XR01 to XR02 was due to mixing (Fig. 1.4).

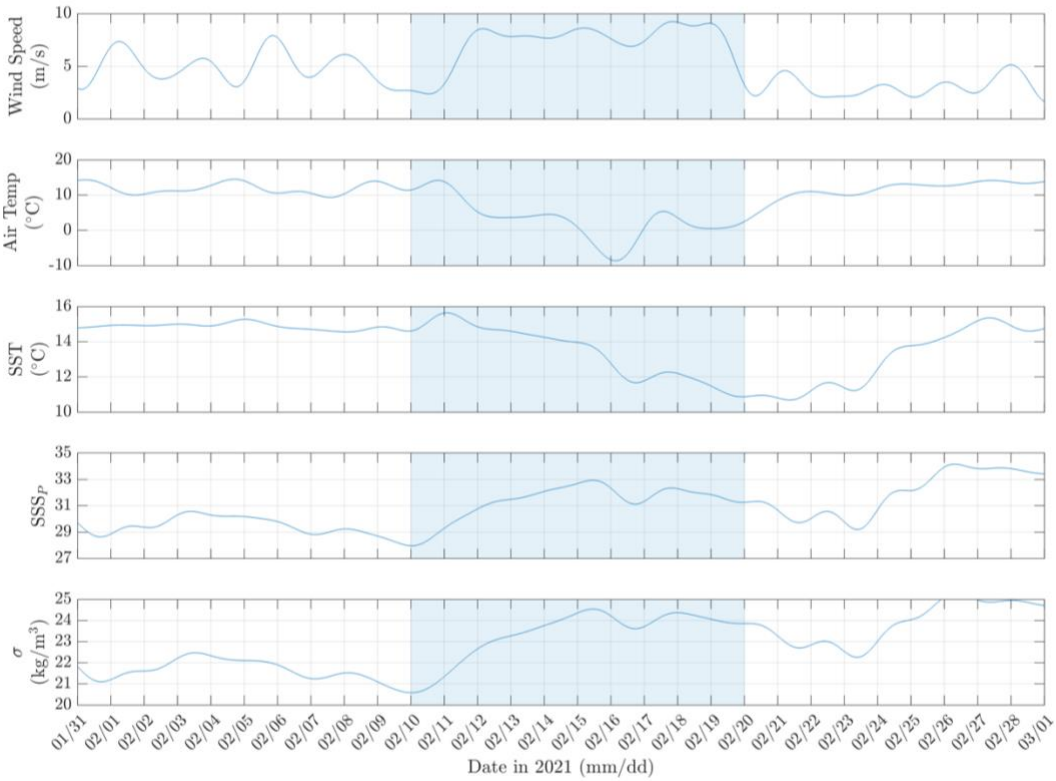

Fig. 1.1. 40-hour Lanczos low-pass-filtered hourly timeseries of wind speed, air temperature, sea surface temperature (SST), sea surface practical salinity (SSS_P), and calculated sea surface density minus 1000 (σ) at Buoy B of the TABS network in February 2021.

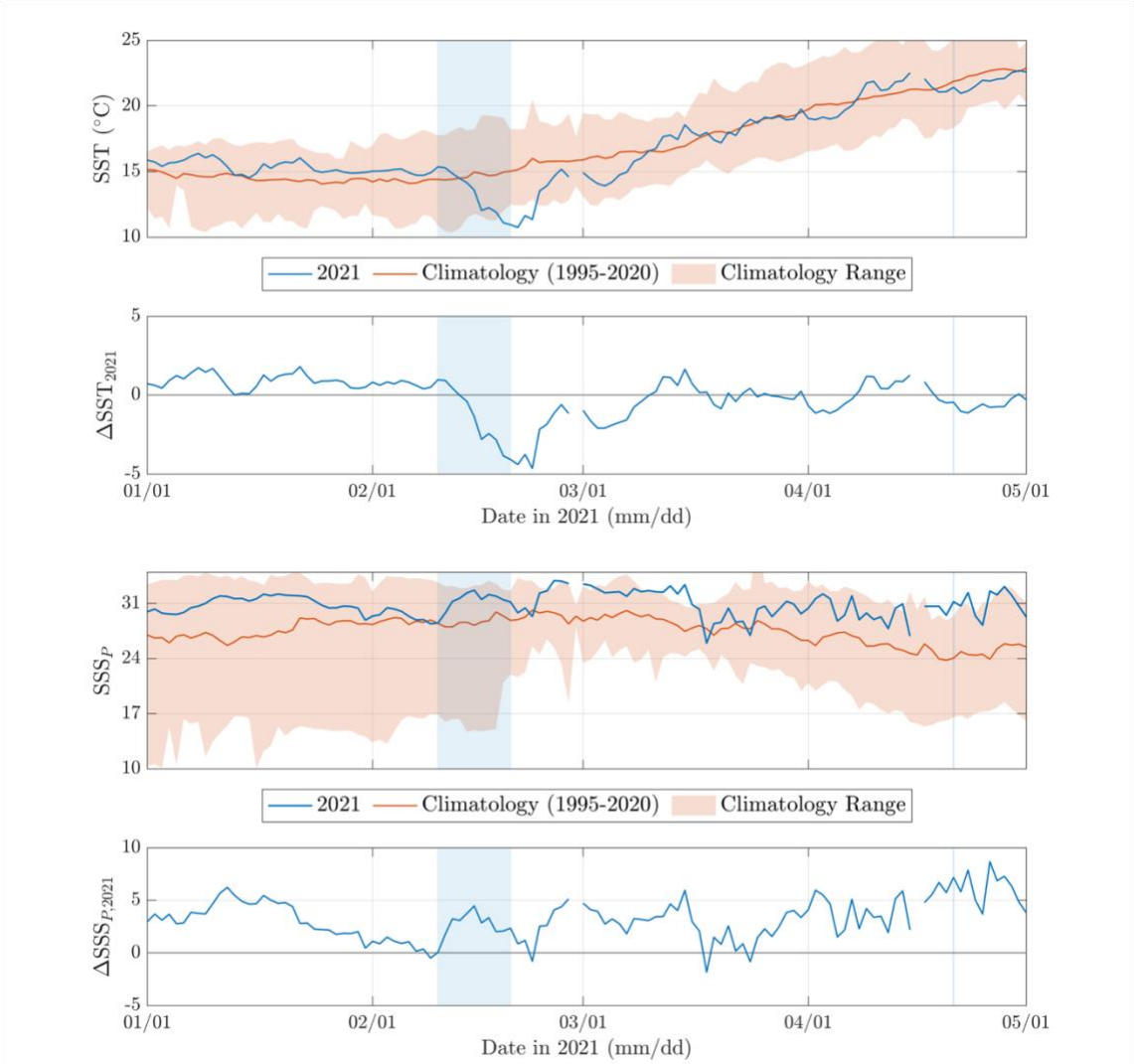

Fig. 1.2. Timeseries and 2021 anomaly plots of sea surface temperature (SST) (top) and sea surface practical salinity (SSS_P) (bottom) from Buoy B of the TABS network. For each hydrographic property, data from 2021 is in solid blue lines, and climatological data averaged over 1995-2020 is in orange lines. The anomaly of the 2021 data with respect to the climatology is shown under the timeseries plots and are calculated as $\Delta a_i = a_{i,2021} - a_{c,i}$ where $a_{i,2021}$ is the SST or SSS_P observation from Buoy B on day i in 2021 and $a_{c,i}$ is the buoy climatology for day i. The datasets are all averaged over each calendar day. The duration of the winter event (February 10-20, 2021) is indicated by the first shaded blue block, and the XR01 cruise date (April 23, 2021) is indicated by the second shaded blue block.

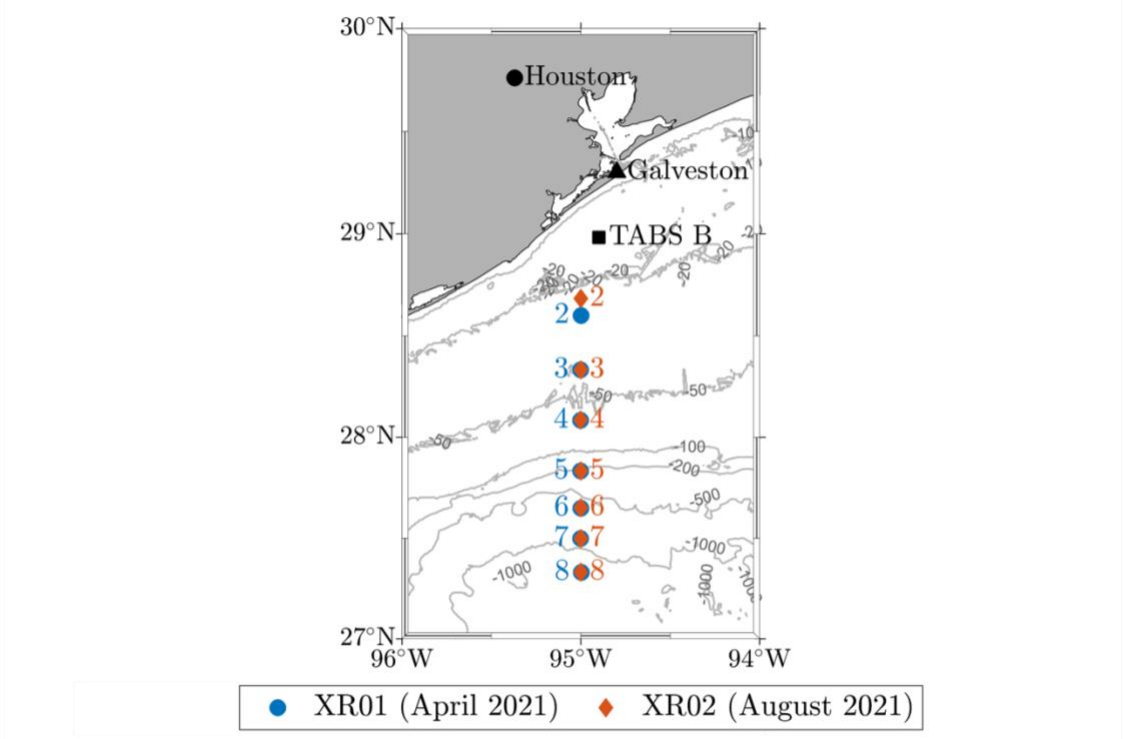

Fig. 1.3. Locations of TABS Buoy B (black square), Galveston (black triangle), Houston (black circle), XR01 stations (blue circles), and XR02 stations (orange diamonds) stations along the GL at 95°W.

Table 1.1. Coordinates of XR01 and XR02 stations along the GL.

Station Number	XR01 (2021-04)		XR02 (2021-08)	
	Lon (°W)	Lat (°N)	Lon (°W)	Lat (°N)
2	94.9982	28.5997	95.0003	28.6833
3	95.0017	28.3322	95.0005	28.3323
4	95.002	28.0837	95.0008	28.0847
5	95.0018	27.8333	95.0002	27.833
6	94.9995	27.6495	94.9997	27.6517
7	95.0012	27.4988	95.0003	27.4992
8	94.9975	27.3312	95.0002	27.3322

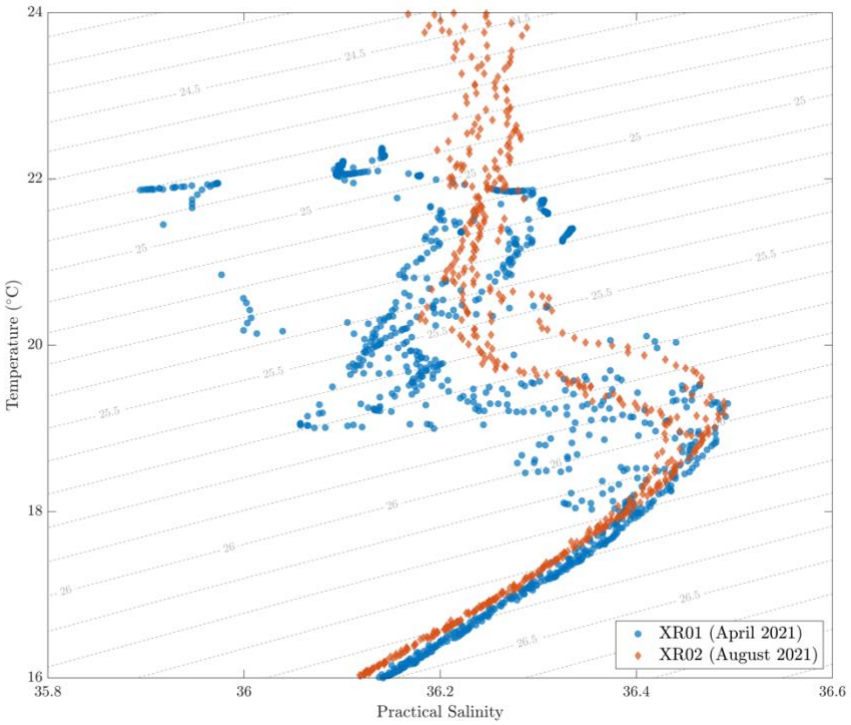

Fig. 1.4. Temperature-Salinity diagram of GL profiles in April and August 2021: XR01 (blue circles) and XR02 (orange diamonds).

1.2. Gulf of Mexico hydrography

1.2.1. Hydrography and coastal water masses in the northwestern Gulf of Mexico

The hydrography in the northwestern Texas-Louisiana (TXLA) shelf is highly influenced by seasonal variability of physical properties: temperature in the region is largely determined by surface heating/cooling and vertical mixing, and salinity is mostly influenced by freshwater input from coastal sources and the advection of offshore water into the region (Cochrane & Kelly, 1986; DiMarco et al., 2005; Nowlin et al., 1998a, 2005). The major source of freshwater in the TXLA shelf is the Mississippi-Atchafalaya River System (MARS) which tends to flow upcoast (eastward) in the summer months and downcoast (westward) the rest of the year, i.e., non-summer months (Cochrane & Kelly, 1986; Zhang et al., 2012). In the northwestern Gulf of

Mexico, the Brazos River also influences salinity values (DiMarco et al., 2012). During the summer months, winds are weak with a westerly component (Wang et al., 1998), allowing the MARS plume to pool within the shelf, which, along with surface heating, intensifies and controls vertical stratification (Nowlin et al., 1998a, 2005). During winter months, atmospheric fronts occur more frequently, and the easterly components of winds intensify (Wang et al., 1998), promoting the downcoast advection of the MARS plume and greater vertical mixing (Nowlin et al., 1998a, 2005).

A study of a numerical model that analyzed SST variability over a nearly 3-decade period identified a cooling trend in the coastal TXLA shelf and a warming trend in the open ocean during winter months, i.e., November to February (Fernández-Nóvoa et al., 2020). The cooling trend was linked to increased MARS plume discharge that in turn increased stratification and promoted surface heat exchange during winter months.

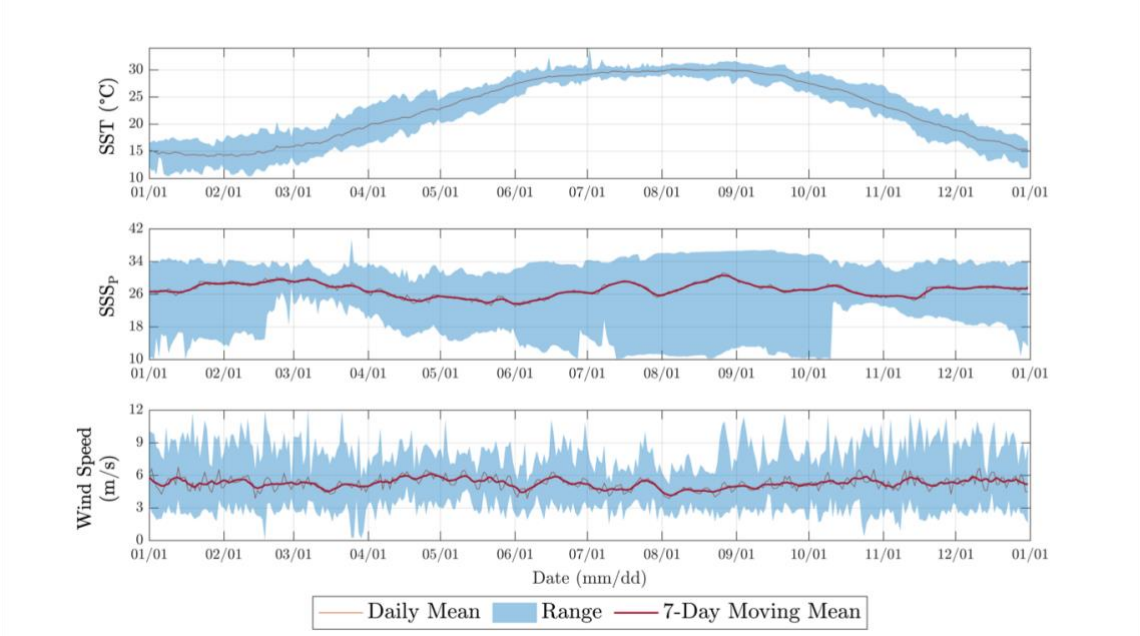

Fig. 1.5. Climatological sea surface temperature (SST), sea surface practical salinity (SSS_P), and wind speed timeseries averaged per calendar day over 16 years (1995-2020) of Buoy B.

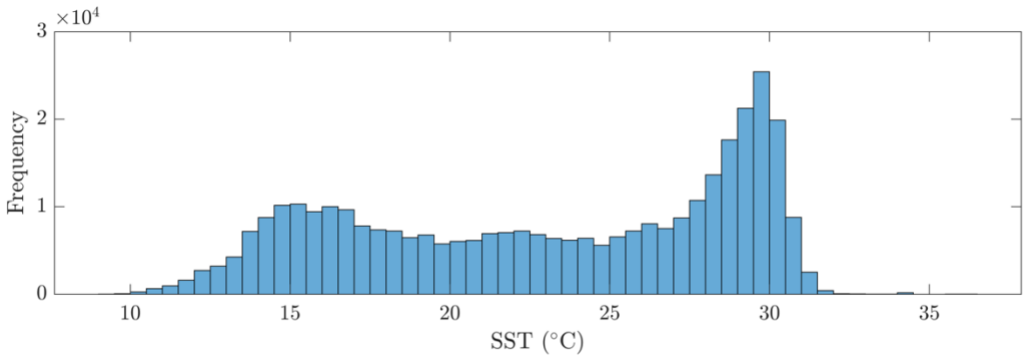

Fig. 1.6. Histogram (bin width 0.5°C) of Buoy B sea surface temperature (SST) from 1995-2020.

1.2.2. Deep water masses in the Gulf of Mexico

Water masses in the Gulf of Mexico are classified by their thermohaline, dissolved oxygen, and other biogeochemical properties, the latter being especially useful in the upper water-column where hydrographic properties overlap (Morrison et al., 1983; Portela et al., 2018). Generally, water mass variability in the Gulf of Mexico is in the upper 250m and is highly influenced by freshwater input via river discharge along the TXLA shelf and by seasonal heat flux (DiMarco et al., 2005; Nowlin et al., 2005; Portela et al., 2018).

The focus in this study is the upper 200 m of the Gulf of Mexico where Caribbean Surface Water, Subtropical Underwater (SUW), Gulf Common Water, and Tropical Atlantic Central Water are present (Cervantes-Díaz et al., 2022). Deeper in the Gulf of Mexico, Antarctic Intermediate Water and North Atlantic Deep Water are also present (Hamilton et al., 2018; Morrison et al., 1983). SUW is characterized by a salinity maximum of ~36.6 at varying depths: ~150-250m according to Morrison et al. (1983), and ~100-150 m according to Hamilton et al. (2018).

1.3. Dense water mass formation and cascading along continental shelves

1.3.1. Dense water mass formation due to cold-air outbreaks

Cold-air outbreaks can significantly modify continental shelf waters by promoting heat exchange and evaporation, resulting in dense water mass formation (Ivanov et al., 2004). Shelf cooling is usually caused by increased heat exchange due to the steep temperature gradient between surface water and the atmosphere but can also occur with increased river discharge. Surface salinity increase can result from upwelling of high-salinity water when winds are upwelling-favorable (Dagg, 1988), or by evaporation when relative humidity is low. Strong winds intensify vertical mixing, with the resulting water-column becoming homogenous and barotropic. Along with cooling, salinity increase, and mixing, a shallow shelf is also conducive to dense water mass formation, as rates of heat exchange are faster in shallower regions due to a smaller heat capacity; this difference affects the water-column response to atmospheric forcing, such that water modification is sudden but shorter-lived in the shallow shelf but longer-lived in the deeper shelf (Nowlin & Parker, 1974; Walker et al., 1987). The temperature difference between surface waters and atmospheric fronts also decreases with distance from the coast as heat exchange occurs, reducing the influence of atmospheric forcing over surface waters with offshore propagation. Additionally, based on the analysis of general circulation model output, surface water temperature has also been shown to influence the propagation speed of cold fronts: warmer temperatures were positively correlated with faster-moving fronts (Passalacqua et al., 2016).

Rapid cooling of shelf waters due to cold-air events has been linked to fish kill-off in the Gulf of Mexico: reports of such events date to 1917 (Finch, 1917), and similar reports along the Texas Coast in Aransas Bay in the 1930s-1950s also exist (Gunter, 1941, 1951). During the

February 2021 winter storms, the sudden drops in SST and prolonged cold temperatures along the TXLA shelf water-column resulted in a large-scale sea turtle cold-stunning event; over 12,000 green sea turtles experienced paralysis due to hypothermia and were found along the Texas coast (Burnett, 2021).

The earliest-known hydrographic survey of the northwestern TXLA shelf which recorded observations from before and during a cold front (Nowlin & Parker, 1974) observed the formation of a dense water mass (~26.7 kg/m^3) in the northwestern TXLA shelf in January 1966. Under the influence of the cold-air outbreak, air temperatures in Galveston reached near-freezing values, and hydrographic properties along the shelf were similar to that of the subsurface SUW (Morrison et al., 1983). Vertical profiles of temperature and salinity obtained during the 15-day outbreak showed that in the presence of strong winds, the water-column along the shelf had become well-mixed and homogenous. Surface water temperatures decreased by almost 5°C and gradients of surface salinity contours had become steeper, increasing values by around 1. Winds during the outbreak are believed to have promoted evaporation and heat exchange, and upwelling and advection of offshore water from the open ocean were deemed unlikely sources of the dense surface water.

1.3.2. Dense water mass cascading and export

Cascading is a process wherein dense water masses along continental shelves may sink down the water-column due to their densities and be transported offshore (Ivanov et al., 2004; Shapiro, 2003; Shapiro & Hill, 1997). During cascading, the dense water masses can flow near or along bottom topography or, if significant mixing with ambient water occurs, achieve neutral buoyancy at shallower depths than the water masses' density compensation depths (i.e., the depths in the water-column where water with the same initial density of the water masses

typically resides). In the Exuma Sound, a shallow (shelf break depth of ~30m) and narrow body of water in the Bahamas, high-salinity plumes were observed to form through year-round evaporation and wintertime surface cooling (Hickey et al., 2000). The plumes were numerically shown to entrain and mix with ambient water as they cascaded down the continental slope. Due to the diapycnal mixing, the plumes reached neutral buoyancy and subducted to just below the mixed layer and could spread laterally along isopycnals.

Cascading is a pathway for exchange between the shelf and the open ocean, and can influence water-column structures of various parameters such as sediment (Canals et al., 2006; Wilson & Roberts, 1995), oxygen (Yoder & Ishimaru, 1989), and phytoplankton (Bernardi Aubry et al., 2018; Vilibić & Šantić, 2008; Yoder & Ishimaru, 1989). Dense water accumulation over several winters during cold-air outbreaks and subsequent offshore cascading have been observed in the Florida and Bahama Banks, and is believed to limit the distribution of coral reefs: export of cold shelf water after multiple cold-air outbreaks resulted in coral mortality events in the 1970s (Porter et al., 1982; Roberts et al., 1982), 1980s (Walker et al., 1982, 1987), and in 2010 (Kemp et al., 2011). Long-term impact of cascading is believed to be reflected in coral reef distributions in the Florida reef tract, wherein coral growth is limited to areas outside of the dense water masses' cascade paths (Walker et al., 1987).

The residence times of the dense water masses on the shelf and initiation of cascading can depend on the frequency of cold-air outbreaks on the shelf (Walker et al., 1987), winds (Walker et al., 1982), and several other factors (Ivanov et al., 2004). Lab experiments have shown that shelf steepness and length also influence the water masses' residence times (Whitehead, 1993).

1.4. Research questions

The goal of this study is to quantify the characteristics (i.e., physical constituents and spatiotemporal evolution and distribution) of the coastal TXLA shelf waters in 2021 and investigate the mechanisms of the formation, movement, and fate of the surface dense water mass during and following the February 2021 Texas winter storms. The key guiding research questions in this study are:

1. What were the main drivers and mechanisms of the formation of the cold dense surface water mass during the February 2021 winter storms?
2. What mechanisms explain the fate of the dense water mass, i.e., the tongue that extended from the surface to the deep seen in the XR01 data and after?

1.5. Scientific hypotheses

To address the research questions and the preliminary analysis of available data, two scientific hypotheses are proposed:

H1. Formation: Strong northeasterly winds during the February 2021 winter storms caused negative heat exchange (heat loss), increased evaporation, and mixing, resulting in the formation of a surface dense water mass in the coastal northwestern Gulf of Mexico, and

H2. Fate: The surface dense water mass that formed during the February 2021 winter storms mixed with ambient seawater, moved offshore past the shelf break, and dissipated by late summer 2021.

H1 is investigated using numerical output from a regional general circulation model to determine the drivers behind the dense water mass formation and objective analysis through a progressive vector diagram. **H2** will be investigated using analysis in TS space, comparison

between 2-D interpolated cross-sections along the GL, volumetric calculation, and numerical output from the GCM and an idealized diffusion model.

1.6. Thesis organization

This thesis is organized into four sections. Section 1 contains background information on the 2021 winter storm event, hydrography and water masses of the Gulf of Mexico, and dense water mass formation and cascading along continental shelves. The motivation for the study, research questions, and hypotheses are also included in this section. Section 2 provides descriptions on the datasets used and methods applied in the analysis. Results and corresponding discussion are presented in Section 3. Finally, Section 4 summarizes the study's findings and provides recommendations for future work.

2. DATA AND METHODS

2.1. Data

This study makes use of six observational datasets that span thirty years (1993-2023), three of which are concurrent with the winter storm events; Table 2.1 contains these datasets and their sources, inclusive dates, and descriptions, and indicates which hypotheses are investigated using each dataset. Fig. 2.1 shows the locations of all stations.

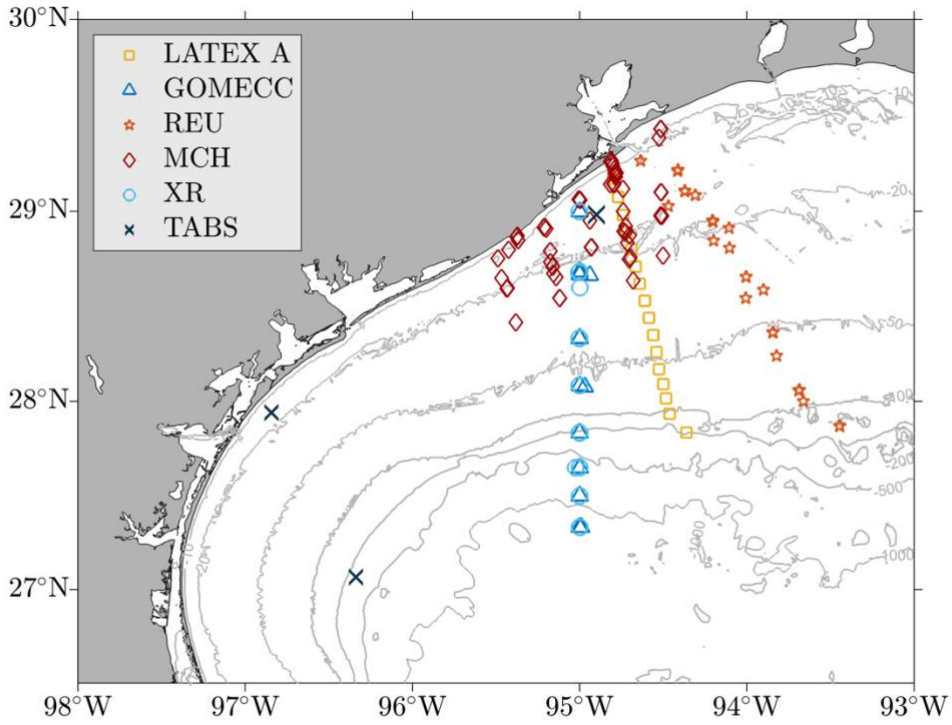

Fig. 2.1. Locations of all observational stations used in this study classified by dataset (Table 2.1).

Table 2.1. Datasets, respective projects, inclusive dates, and descriptions used in this study.

Dataset Number	Dataset Name	Project/s and Funding	Inclusive years	Description of Observational Data or Model Output	Hypothesis investigated
1	XR Cruise Data	NOAA Ocean Acidification Program: Ocean Acidification on a Crossroad: Enhanced Respiration, Upwelling, Increasing Atmospheric CO_2, and their interactions in the northwestern Gulf of Mexico	2021-2023	36 total CTD casts 12,747 datapoints	**H1**
2	GOMECC	NOAA Ocean Acidification Program: Gulf of Mexico Ecosystems and Carbon Cycle Cruises: GOMECC-1 (Langdon & Rosenstiel School of Marine and Atmospheric Science, 2011) GOMECC-3 (Barbero et al., 2019) GOMECC-4 (Wanninkhof et al., 2021)	2007, 2017, 2021	25 total CTD casts 2,871 datapoints	**H2**
3	LATEX A	Minerals Management Service – Department of the Interior (MMS-DOI): Louisiana-Texas Shelf Oceanography Program A (DiMarco et al., 1997; Nowlin et al., 1998a, 1998b)	1993-1994	65 total CTD casts 4,178 datapoints	**H2**
4	TABS	Texas General Land Office: Texas Automated Buoy System (http://tabs.gerg.tamu.edu)	1995-2020	Meteorological and hydrographic timeseries from Buoys B, D, and X	**H1, H2**
5	REU	National Science Foundation - Research Experience for Undergraduates (REU): Observing the Ocean Award numbers: 1455851, 1849932	2016, 2018, 2019	24 total CTD casts 1734 datapoints	**H2**
6	MCH	NOAA Center for Sponsored Coastal Ocean Research: Mechanisms Controlling Hypoxia (MCH) Grant numbers: NA03N0S4780039, NA06N0S4780198, NA09N0S4780208	2010-2014	80 CTD casts 309 datapoints	**H2**
7	Regional General Ocean Circulation Model	R-CESM: Regional Community Earth System Model (Fu et al., 2021)	2021	Temperature, salinity 51 depth bins (0-500m, 10m intervals) Data output every 6 hours	**H1, H2**
8	Idealized Diffusion Model	N/A	2021	Temperature, practical salinity	**H2**

2.1.1. Observational data

For all datasets used in this study, temperature and practical salinity observations were collected at each station at various depths. Practical salinity (S_P) is calculated from conductivity measurements using the Practical Salinity Scale of 1978 (UNESCO, 1981) and following the TEOS-10 guidelines (McDougall & Barker, 2011). S_P is expressed as a unitless quantity.

This study uses hydrographic profiles along the GL collected over three years during the XR cruises: XR01(April 2021), XR02 (August 2021), XR03 (October 2022), XR04 (December 2022), and XR05 (March 2023). We compare these profiles with each other and with the climatology composed of datasets 2 to 6 (Table 2.1) to investigate the hydrographic impact of the winter storm and seasonal variability along the GL.

Observations from the TABS network (Buoys B, D, and X) funded by the TGLO are available from 1995 and provide in-situ meteorological and oceanographic observations for state-mandated oil spill response and mitigation policy (http://tabs.gerg.tamu.edu and http://gcoos.org). In this study, we use TABS buoys' historical surface hydrography to establish the climatology along the northwestern Gulf of Mexico and hydrographic and meteorological conditions during the winter storm. This allowed us to assess the impact that the winter storm had on the surface waters at Buoy B.

The datasets we use to establish the climatology in this study span three decades (1993-2023). The 2007 and 2017 transects along the GL line from the GOMECC project contribute to the coastal and offshore climatology, while the 2021 transect is compared with XR01 and XR02 to investigate the spatiotemporal evolution of the subductive tongue in XR01. Profiles from the LATEX project and the REU cruises near the GL (Fig. 2.1) span five years (1993-1994 and 2016, 2018, and 2019 respectively) and also make up the climatology of the region extending

offshore. Hydrographic profiles from the MCH project establish the coastal climatology for 2010-2014.

Geographical maps were generated with the MATLAB package **m_map** (Pawlowicz, 2020) using colormaps from **cmocean** package (Thyng et al., 2016).

2.1.2. Numerical data

To investigate high-frequency spatiotemporal variability and to fill in gaps in observational parameter space, we used numerical models to simulate the formation of the dense water mass and to investigate the mechanisms behind its eventual fate. Two sets of numerical output are used in this study:

1. The output from a 3-km resolution regional general circulation model (GCM) from the Regional Community Earth System Model or R-CESM (Fu et al., 2021) using the Japanese 55-year Reanalysis (JRA-55: Japanese 55-Year Reanalysis, Daily 3-Hourly and 6-Hourly Data, 2013) for atmospheric forcing and the Copernicus Marine Environment Monitoring Service (CMEMS) Global Ocean 1/12° Physics Analysis and Forecast Analysis (Lellouche et al., 2018) for initial and boundary conditions. The GCM is run from 01 February 2021 to 21 April 2021. The GCM does not include direct river discharge forcing, but seasonal variability in river input is incorporated in the climatological hydrography of the GCM.

   The GCM was used to examine the temporal evolution of hydrographic properties along the GL before and under the influence of the winter storms, and to qualitatively assess the main atmospheric and/or oceanic processes that led to the formation of the dense water mass.

2. The output of an idealized diffusion model run using the XR05 temperature and salinity transects to relate spatiotemporal scales of diffusion to observed shelf conditions.

2.2. Methods

2.2.1. Data analysis

For continuous timeseries used in this study, we used a 40-hr Lanczos cosine low-pass filter to eliminate high-frequency variability, leaving only the variance associated with frequencies equal to or lower than 1 cycle/40 hours (Thomson & Emery, 2014). For discontinuous timeseries, values within each calendar day were averaged.

We performed 2-D linear interpolation with the MATLAB function **griddata** (*MATLAB Version: 9.13.0 (R2022b)*, 2023) on the GL profiles from XR01 (April 2021), XR02 (August 2021), and XR05 (March 2023) to create temperature, salinity, and density cross-sections; calculation parameters included a grid of horizontal spacing dx = 0.01°latitude = 1100m and vertical spacing dz = 1m. The differences between XR05 and XR01 cross-sections were analyzed to investigate the anomaly of the XR01 transect.

2.2.2. Volumetric calculation of the water mass

We performed a 3-dimensional volumetric calculation of the 2021GL hydrography from XR01 and XR02 using the 2-D cross-sections of density (Section 2.2.1), assuming a cross-section meridional width of 1m. To investigate the fate of the dense water mass between April and August 2021, we defined the density range of the water mass (σ_{WM}) to be 1025.2 – 1025.8kg/m^3. The minimum value of this range was determined by the maximum density recorded by the nearshore TABS buoys in February 2021; this value was assumed to be the initial density of the water mass during formation, before significant mixing had occurred. The maximum value in this range was determined from the top of the permanent pycnocline of the

hydrography in the region (Fig. 1.4), where points from the climatological data and the XR cruises begin to overlap in TS space.

2.2.3. Progressive vector diagram (PVD)

Hourly PVDs (Thomson & Emery, 2014) at TABS Buoys B, D, and X (Fig. 3.9) show the spatiotemporal evolution of SST and SSS_P for the date range 10-16 February 2021 and aid in assessing the hydrographic conditions during the winter storm event. This date range coincided with the observed salinity increase at Buoy B (Fig. 1.1).

2.2.4. Numerical modeling of idealized diffusion

We wrote a 2-dimensional idealized diffusion model to analyze the mechanisms and the factors that control the dynamics of the water mass. The model projects diffusion along isopycnals using the Redi Scheme (Redi, 1982) which involves a coordinate transformation using a rank-2 tensor K_{redi}:

$$K_{redi} = \begin{bmatrix} 1 & m_x \\ m_x & |m_x|^2 \end{bmatrix},$$

where m_x is the ratio of the density (σ) gradients along the horizontal (x) and vertical (z) directions, i.e.,

$$m_x = -\frac{\partial\sigma/\partial x}{\partial\sigma/\partial z}.$$

For a given property c, the modified advection-diffusion equation is

$$\frac{dc}{dt} = \kappa_\rho \nabla \cdot K_{redi} \nabla c - (u \cdot \nabla c) + \kappa_V \frac{\partial^2 c}{\partial z^2},$$

where κ_ρ is the isopycnal diffusivity coefficient, and dc/dt is calculated for both temperature T and salinity S. In this study, $\kappa_\rho = 600 m^2/s$ and $\kappa_v = 0.001 m^2/s$ for both T and S. We perform convective adjustment, such that κ_v increases to $0.01 m^2/s$ if denser water is sitting on top of lighter water. The XR05 2-D linearly interpolated GL cross-sections of temperature and salinity

initialized the model. To simulate the conditions during the winter storms, we applied a $\tanh(\circ)$ function to the temperature transect along the continental shelf, lowering the temperature and consequently increasing the density. We then performed optimal interpolation (S.F. DiMarco, personal communication, May 5, 2023; Wilkin et al., 2002) to extrapolate both transects to bottom topography, and developed a land mask based on the bottom depths of the XR05 transect profiles. We assume that the model is a cross-section of an infinitely long water-column that is uniform with latitude and depth. The model was run for 2 weeks with a timestep $\mathrm{dt} = 1$ second.

Finally, to aid in data visualization, we smooth the cross-sections using the MATLAB function **smoothdata** (*MATLAB Version: 9.13.0 (R2022b)*, 2023) with a Gaussian-weighted moving average of a window size of 1,100m along latitude, and then along depth with a window size of 10m.

3. RESULTS AND DISCUSSION

Section 3.1.1 presents the analyses from the XR01, XR02, and XR05 cruises as cross-sections of temperature, salinity, and density (Fig. 3.1 to Fig. 3.3), and provides quantitative comparison between these variables in the XR05 and XR01 cross-sections (Fig. 3.4) and with climatological conditions of the region. TS analysis of the XR01, XR02, and GOMECC4 cross-sections (Fig. 3.5) and all GL profiles (Fig. 3.6 and Fig. 3.7) is found in Section 3.1.2, and the volumetric calculation of the water mass during XR01 and XR02 (Fig. 3.7 and Fig. 3.8, Table 3.1) in Section 3.1.3. Section 3.1.4 investigates the potential source of the salinity increase recorded at Buoy B (upper TXLA coast) during the winter storm event (Fig. 1.1) with hourly PVDs of Buoys B, D (mid-TXLA coast), and X (offshore Texas) (Fig. 3.9) that summarize the current direction, SST, and SSS_P from 10-16 February 2021. In Section 3.2, we provide a description of the formation mechanisms of the dense water mass (Hypothesis **H1**). In Section 3.2.1, we compare surface temperature and salinity measurements from the GCM with the Buoy B timeseries (Fig. 3.10) to investigate the driver/s of the modifications to surface ocean properties during the winter storms. The temporal evolution of the GL in the GCM before and during the winter storm is presented in TS space in Section 3.2.2 (Fig. 3.11). Finally, Section 3.3 contains the results of the idealized diffusion model (Fig. 3.12 to Fig. 3.15).

3.1. GOMECC Galveston Line (GL) cross-sections

3.1.1. Multi-year seasonal GL cross-section comparison

Across the western TXLA shelf, the cross-shelf spatial scale of hydrographic properties is ~15km (Li et al., 1996), i.e. temperature and salinity measurements become decoupled at this distance between observation points. This applies to the XR01 water mass (Fig. 3.1) that extends

from the shelf break at ~28°latitude to the open ocean at ~27.5°latitude along a distance of ~0.5°latitude = ~55.5km.

Fig. 3.1 to Fig. 3.3 show high-resolution cross-sections along the GL during the XR01, XR02, and XR05 cruises. In the XR01 (Fig. 3.1) salinity cross-section, there is a subductive tongue: a water mass in the upper 60m defined by the 36.2 isohaline extending seaward and beneath the 22°C mixed layer at around 30m. XR01 has temperatures T in the range $17°C \leq T_{XR01} \leq 23°C$ and densities σ within the range $24.9kg/m^3 \leq \sigma_{XR01} \leq 27.1\ kg/m^3$. In XR02 (Fig. 3.2), temperature and density ranges are $17°C \leq T_{XR02} \leq 30°C$ and $19kg/m^3 \leq \sigma_{XR02} \leq 27.1kg/m^3$ respectively. Surface warming and fresher surface waters due to summertime accumulation of river discharge from spring snow melt upstream and increased precipitation in the northwestern Gulf of Mexico result in XR02 practical salinities of $S_{P,XR02} < 36$ in the upper 30m. In the XR02 salinity cross-section, the subductive tongue had diminished, as practical salinities $S_P = 36.2$ are not present in the upper 30m (Fig. 3.2). For both cross-sections, the S_P maximum of ~36.45 to >36.5, corresponding to the SUW, is between 100 – 150m.

XR05 cross-sections (Fig. 3.3) show a nearshore plume of relatively low salinity ($S_P <$ 36) from the surface to ~25m above higher salinity water. A high-density water mass bounded by a $26kg/m^3$ isopycnal deepens with distance from the coast from ~15m to ~60m along the continental shelf; past the shelf break (latitudes < 28.1°), the isopycnal is at ~90m. The $26kg/m^3$ isopycnal was at ~60 – 80m in XR02 (Fig. 3.2) and 80 – 90m in XR01 (Fig. 3.1).

Isopycnals in the density range $25.2\ kg/m^3 \leq \sigma_{WM} \leq 25.8kg/m^3$ converge at the base of the mixed layer in XR01 (Fig. 3.1). The vertical gradient of density becomes steeper with seaward movement along the cross-section: at 28.2°latitude, a change in density $\Delta\sigma = +0.3kg/m^3$ (27.2 kg/m^3 to 27.5 kg/m^3) takes place over 30m in the water-column, whereas at 27.65°latitude the

same density increase takes place over ~5m. This vertical gradient in the open ocean results in stronger stratification and therefore inhibits vertical mixing. We see a large vertical gradient in the XR02 density cross-section (Fig. 3.2) at depths >60m where density increases by ~0.2 kg/m^3 every 5m, at which point the signal of the water mass had diminished.

The first-order difference (referred to with the subscript "XR05-XR01") between XR05 (early March 2023) and XR01 (late April 2021) cross-sections (Fig. 3.4) show varying trends along the continental shelf (latitudes > 28°N) and in the open ocean (latitudes < 28°N). Along the continental shelf, XR01 is fresher ($\Delta S_{P,\ XR05\text{-}XR01} > 0$) (except for at the surface corresponding to the plume of $S_P < 36$), warmer ($0°C \leq \Delta T_{XR05\text{-}XR01} \leq +4°C$), and less dense ($-0.8 kg/m^3 \leq \Delta\sigma_{XR05\text{-}XR01} \leq 0 kg/m^3$) than XR05. In the open ocean, XR01 is still fresher ($\Delta S_{P,\ XR05\text{-}XR01} > 0$), generally colder ($-2°C \leq \Delta T_{XR05\text{-}XR01} \leq 0°C$), and denser ($0 kg/m^3 \leq \Delta\sigma_{XR05\text{-}XR01} \leq +0.4 kg/m^3$) in the depth range of ~40 – 90m.

The isopycnal convergence in the XR01 cross-section (Fig. 3.1) is evidence of the offshore movement of the water mass and its mixing with ambient water as it cascades. Conservation of mass points to the more likely scenario that the water mass originated from the continental shelf and moved offshore, eventually forming the subductive tongue as opposed to the converse scenario where the water mass originates in the open ocean and increases in its vertical extent with onshore movement. If we assume that the initial density of the water mass was greater than that of the upper mixed layer (25.2 kg/m^3), then the density range of the water mass σ_{WM} being a subset of the larger range bounded by the densities of the mixed layer and the deep ocean, i.e. $25.2 kg/m^3 \leq \sigma_{WM} \leq 26 kg/m^3$, indicates diapycnal mixing with ambient water.

This is similar to numerical results from Hickey et al. (2000) where surface dense water masses mixed with and entrained ambient water while cascading and eventually subducted under

the mixed layer where they reached neutral buoyancy and spread laterally. Lateral or meridional spreading along longitudes across surfaces of constant density may account for the conservation of mass in the converging isopycnals beneath the upper mixed layer.

Because XR05 was conducted in the winter and XR01 in the spring, we expect the XR05 water-column to be generally denser than XR01's due to wintertime atmospheric cooling and evaporation and downcoast advection of freshwater (Cochrane & Kelly, 1986). However, Fig. 3.4 shows that XR01 is denser than XR05 by up to $+0.4 kg/m^3$ offshore (depths ~40m – 90m) in a region that contains the location of the subductive tongue and beneath it (Fig. 3.1). This alignment between the subductive tongue region with an area of higher density during XR01 ($25.7 kg/m^3 \leq \sigma_{XR01} \leq 26.2 kg/m^3$), despite the aforementioned expected seasonal difference of a colder and saltier water-column during XR05, is consistent with the XR01 cross-section being anomalous due to the water mass cascading (Hypothesis **H2**).

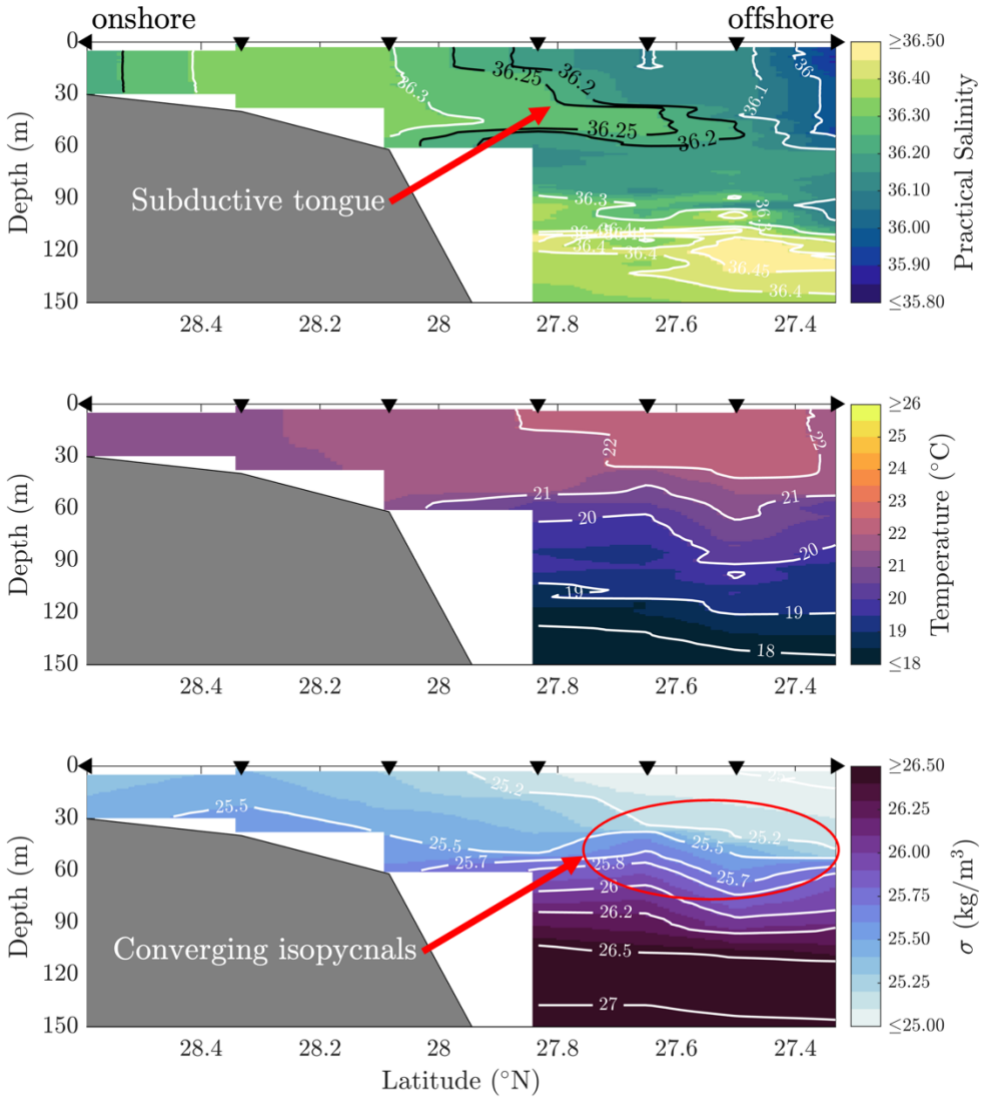

Fig. 3.1. Cross-sections of XR01 (April 2021) profiles along the GL of practical salinity (top), temperature (middle), and density minus 1000 (σ) (bottom). Black triangles are data collection latitudes: downward-facing triangles are located within the cross-section bounds and rotated triangles are outside of the bounds at 28.6°N and 27.33°N. The subductive tongue in the salinity cross-section (~36.2 in black) is seen subducting under the 22°C mixed layer. Converging isopycnals in the offshore density cross-section is highlighted.

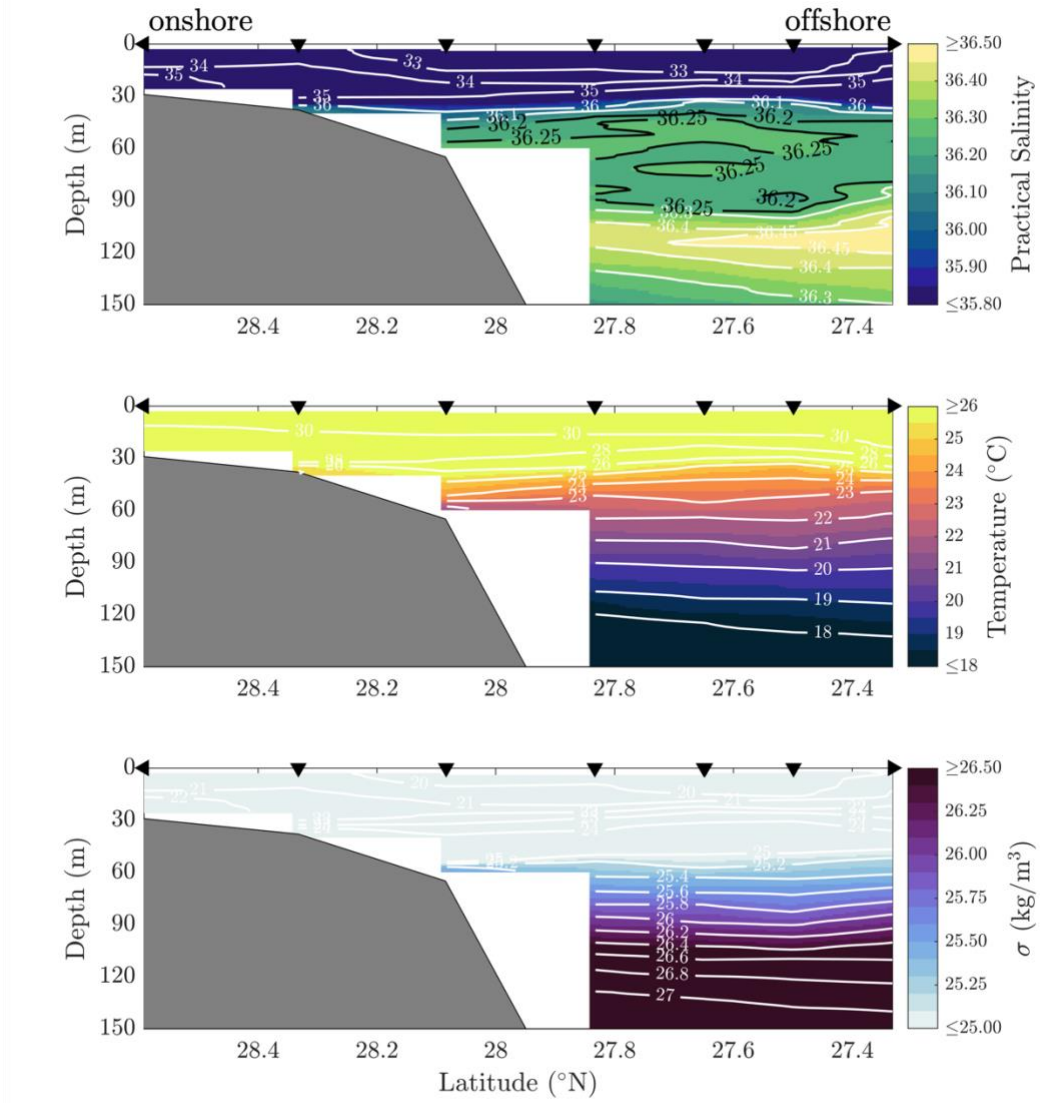

Fig. 3.2. Cross-sections of XR02 profiles (August 2021) along the GL of practical salinity (top), temperature (middle), and density minus 1000 (σ) (bottom). Black triangles are data collection latitudes: downward-facing triangles are located within the cross-section bounds and rotated triangles are outside of the bounds at 28.68°N and 27.33°N.

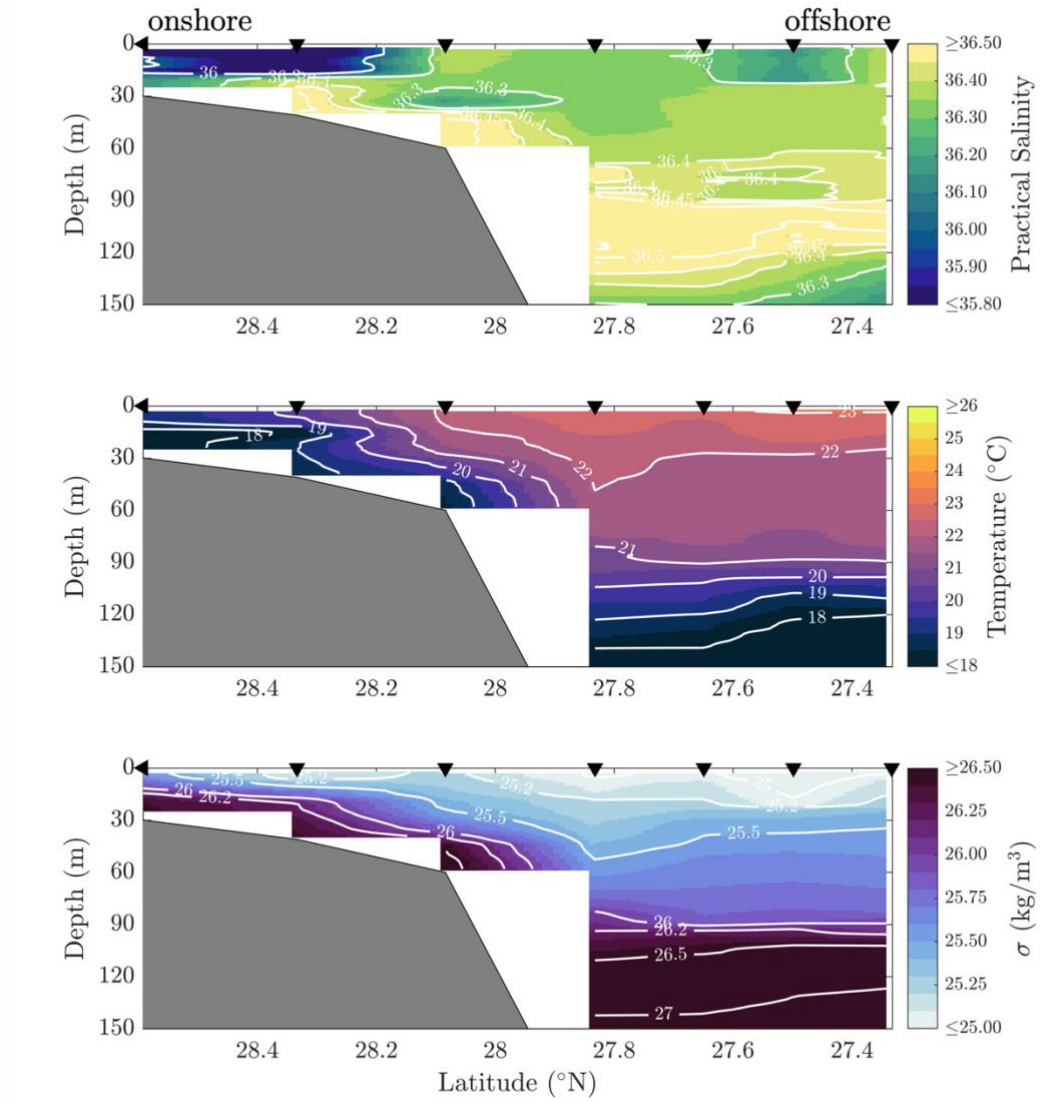

Fig. 3.3. Cross-sections of XR05 (March 2023) profiles along the GL of practical salinity (top), temperature (middle), and density minus 1000 (σ) (bottom). Black triangles are data collection latitudes: downward-facing triangles are located within the cross-section bounds and the rotated triangle is outside of the bounds at 29°N.

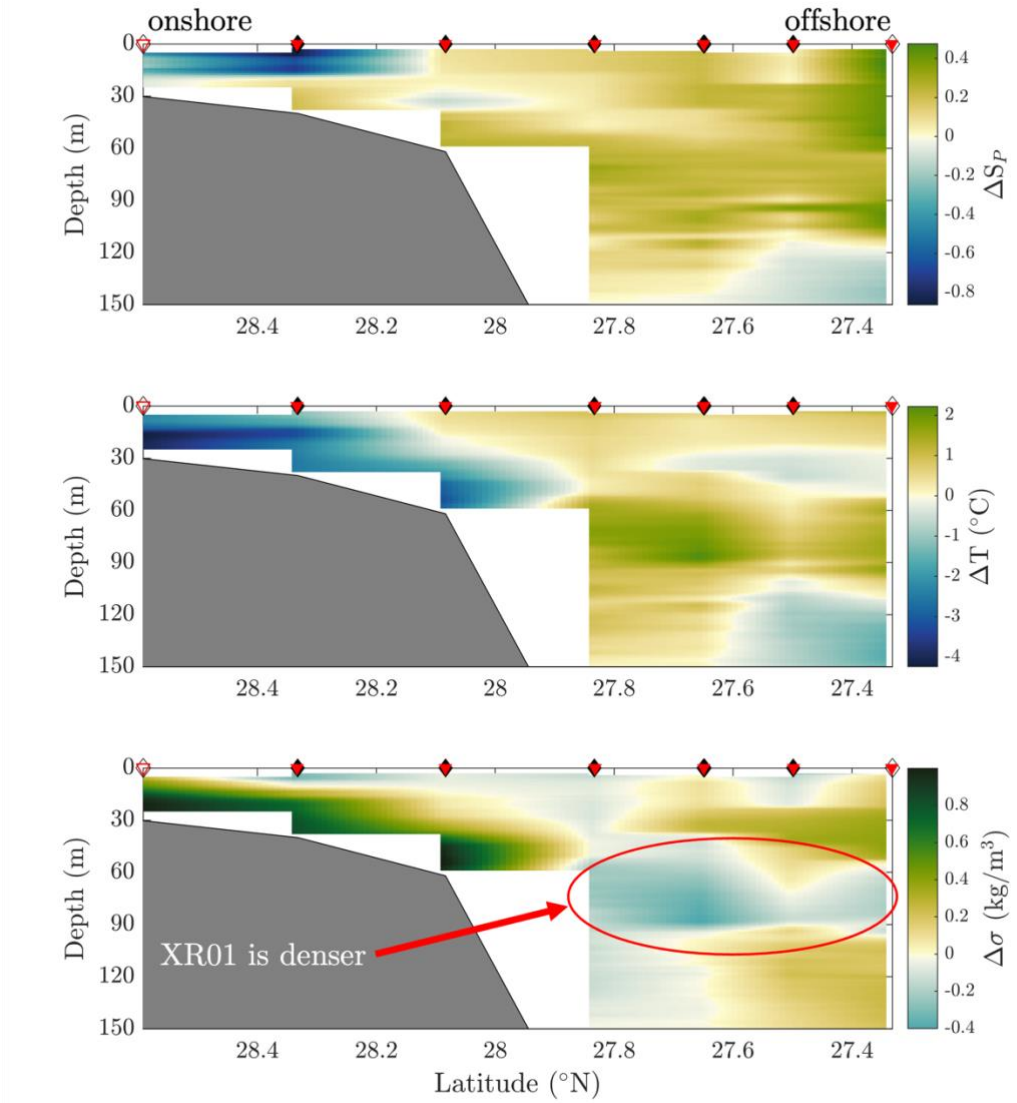

Fig. 3.4. First-order difference (Δ) between the cross-sections of XR05 (Fig. 3.3) and XR01 (Fig. 3.1) along the GL of practical salinity (S_P) (top), temperature (T) (middle), and density minus 1000 (σ) (bottom). Black diamonds and red triangles are data collection latitudes of XR01 and XR05 respectively; solid shapes are located within the cross-section bounds and hollow shapes are outside the bounds (XR01: 28.6°N and 27.33°N, XR05: 29°N).

3.1.2. Analysis in Temperature-Salinity (TS) space

Along with the TS profiles of XR01 and XR02 (Fig. 1.4), GOMECC 4 profiles show the evolution of the hydrography of the northwest Gulf of Mexico near Galveston, Texas.

In Fig. 3.5, TS profiles of XR01, XR02, and GOMECC4 above the 26.2kg/m^3 isopycnal have temperatures within the range 17°C ≤ T ≤ 26°C and practical salinity values within the range 35.8 ≤ S_P ≤ ~36.5; TS values below this density correspond to deep-water hydrography along the GL where seasonal variability between the three cruises is minimal. Fig. 3.6 shows all GL profiles from 2021-2023 and the climatology in the area (Table 2.1). In both figures, the density range of 25kg/m^3 – 26.5kg/m^3 used in the cross-sections (Fig. 3.1 to Fig. 3.3) are highlighted.

There is a sharp curve in the XR01 profiles that deviates from the climatology and other GL profiles characterized by a distinct density anomaly along the 25.7kg/m^3 isopycnal with a practical salinity minimum between 36 and 36.1 at ~19°C. In the XR02 profiles, there is a similar curve that also deviates from the climatology but is not as sharp; it is located along the 25.4kg/m^3 isopycnal with a practical salinity minimum between 36.1 and 36.2 at ~20°C. By GOMECC4, the curve is still present but weakened even further along the ~25.1kg/m^3 isopycnal with a practical salinity minimum > 36.2 at ~21.5°C. Therefore, from April (XR01) to September (GOMECC4) 2021, the salinity minima of the curves became saltier ($\Delta S_{P,min}$ = ~+0.2) and warmer (ΔT = ~+2.5°C), and so the density anomaly of the curves became less dense ($\Delta\sigma$ = -0.6kg/m^3).

The XR01 and XR02 profiles deviate from the hydrography of all other GL profiles and the climatology along their distinct curves (Fig. 3.6). Above 26.2kg/m^3, XR01 profiles have a smaller temperature range (~17.5 – 22°C) in comparison to XR02 profiles; this range is similar

to that of XR05 profiles, but are relatively fresher ($S_{P,min,XR01} \geq$ ~35.9, $S_{P,min,XR05}$ = ~36.1 during XR05, except for a few outliers).

The decreasing density of the salinity minima of each successive curve from XR01 to GOMECC4 ($\Delta\sigma_{XR01\ to\ GOMECC4}$ = -0.6kg/m^3) indicates that the water mass mixed with and entrained ambient water from April to September 2021 during cascading (Hypothesis **H2**). The changes in density along the GL during this time were controlled by temperature; the salinity minimum increased by ~0.2, but its temperature increased by ~2.5°C. Furthermore, the locations in the water-column of the points that make up the XR01 sharp curve are contained within the region under the subductive tongue in the XR01 salinity cross-section (Fig. 3.1) where XR01 water was denser than XR05 by 0.4kg/m^3 (Section 3.1.1, Fig. 3.4). As in the previous section, this alignment, along with the interpretations of profiles in TS space and the distinct differences between the XR01 and XR02 profiles and the other GL cross-sections and climatology (Fig. 3.6), are consistent with the water mass's fate of mixing in **H2** and supports the anomalous nature of the XR01 subductive tongue.

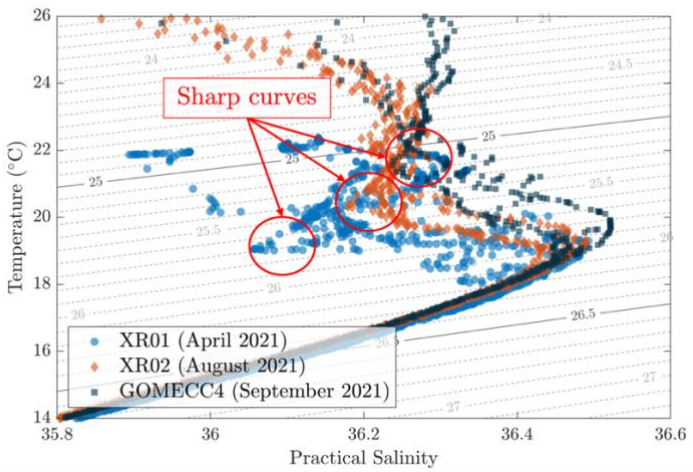

Fig. 3.5. Temperature-Salinity diagram of GL profiles in 2021: XR01 (blue circles), XR02 (orange diamonds), and GOMECC4 (dark blue squares). Red arrows and circles point out the salinity minima of each sharp curve. The density range in the cross-sections (Fig. 3.1 and Fig. 3.2) of 25.0kg/m^3 – 26.5kg/m^3 is highlighted.

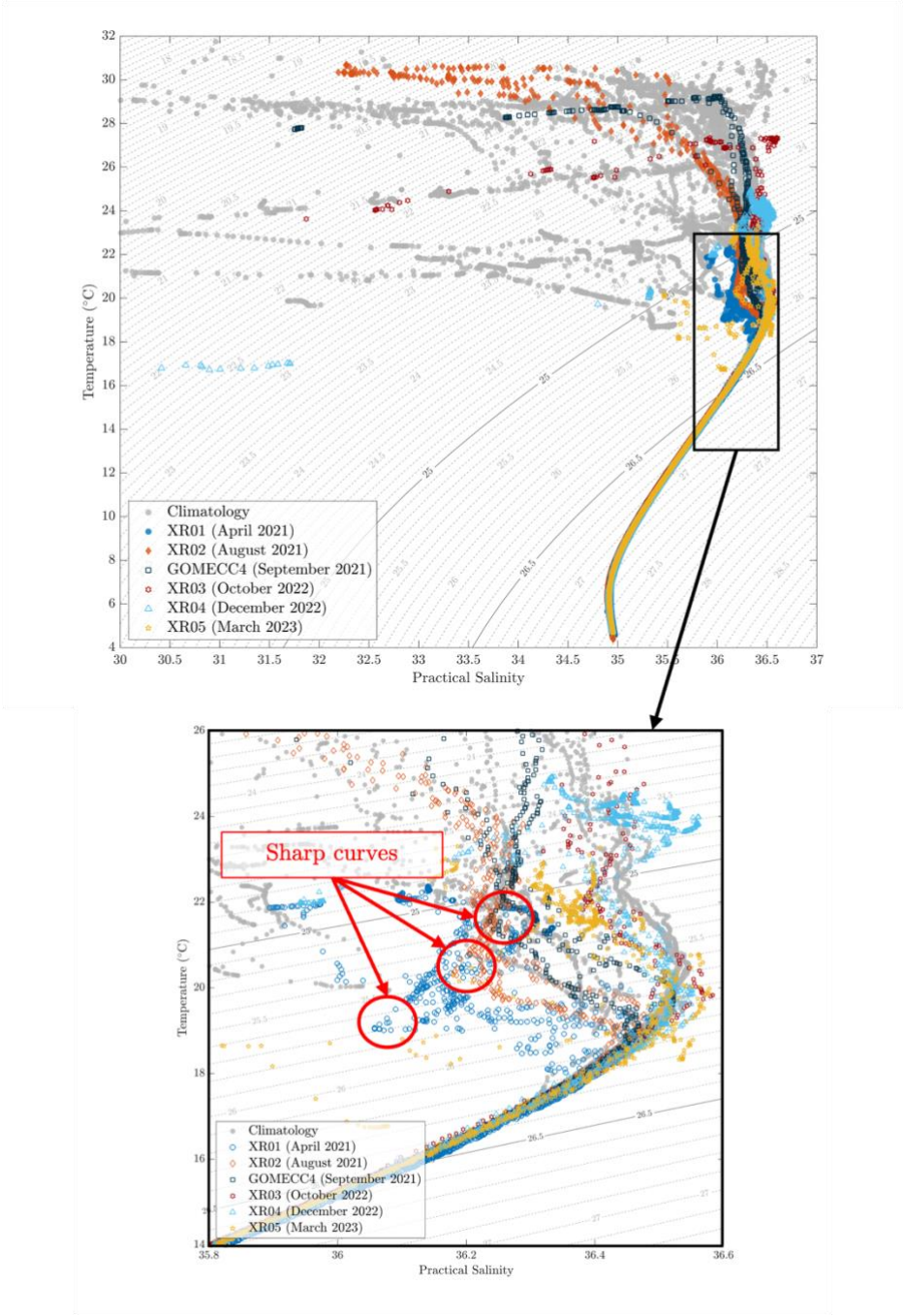

Fig. 3.6. Temperature-Salinity diagram of climatology, XR cruises, and GOMECC4 cruise profiles along the GL profiles for the entire TS range (top) and zoomed into the area of mixing (bottom). Climatology is composed of data from Table 2.1. Red arrows and circles point out the sharp curves in XR01, XR02, and GOMECC4. The density range in the cross-sections (Fig. 3.1 and Fig. 3.2) of 25.0kg/m^3 – 26.5kg/m^3 is highlighted.

3.1.3. Volumetric calculation of the dense water mass

Defining the dense water mass to be within the range in Section 2.2.2 ($25.2 kg/m^3 \leq \sigma_{WM} \leq 25.8 kg/m^3$) and assuming a cross-meridional width of 1m, we estimated the total volume of the water mass within the cross-sections (Fig. 3.1 and Fig. 3.2). Fig. 3.7 shows the representation of this calculation in TS space, where each colored box represents a count n times a volume along the GL with size 0.01°latitude × 1m × 1m, where 1°latitude = 111km. For example, using the same colorbar in Fig. 3.7, a yellow box corresponds to a count *n*, $1125 \leq n < 1250$, such that the volume of water with the hydrographic properties within the range of the box is $n \times 111{,}000 m^3$. A histogram of water densities found in XR01 and XR02 is shown in Fig. 3.8.

Within the selected temperature and practical salinity limits in Fig. 3.7 ($15°C \leq T < 27°C$, $34.6 \leq S_P < 37$) the XR01 ranges (T_{XR01}, $S_{P,XR01}$) are smaller than those of XR02 (T_{XR02}, $S_{P,XR02}$): $15°C \leq T_{XR01} < 23°C$ and $15°C \leq T_{XR02} < 27°C$, and $35.8 \leq S_{P,XR01} \leq 36.4$ and $35.4 \leq S_{P,XR02} \leq 36.4$. This results in a larger volume of water during XR01 than XR02 within 21°C – 22°C and 36.2 –36.3 practical salinity.

Water at temperatures >22°C and $36.1 \leq S_P \leq 36.2$ corresponds to the XR01 mixed layer seen in Fig. 3.1. The intersection of the dashed red boxes in Fig. 3.7 ($19°C \leq T \leq 20.5°C$, $36 \leq S_P \leq 36.2$, $25.2 kg/m^3 \leq \sigma \leq 25.8 kg/m^3$), which corresponds to the hydrographic range of the XR01 curve from Section 3.1.2 (Fig. 3.5 and Fig. 3.6), shows that there is a higher count of water parcels not only in the density range σ_{WM} but within the TS ranges of the XR01 curve. This is also seen in the results of the calculation in Table 3.1 and in the histogram of densities in Fig. 3.8: in XR01, the water mass made up 33.89% of the cross-section along the GL and densities in the upper water-column were concentrated in the 25 kg/m^3 – $25.6 kg/m^3$ range, and by August,

this had reduced to 10.46% and the range of upper water-column densities was larger, extending to densities <23kg/m^3.

The larger volume of water found within σ_{WM} during XR01 in comparison to during XR02 and the reduction in volume of water within the XR01 curve TS range from XR01 to XR02 points to mixing along the GL between these two cruises, substantiating hypothesis **H2**. Paired with the TS analysis from Section 3.1.2, these results show that the water mass's evolution from April to August 2021 involved diapycnal mixing with ambient water as the water mass cascaded. This resulted in the water mass sinking to depths much shallower than its density compensation depth (Hickey et al., 2000).

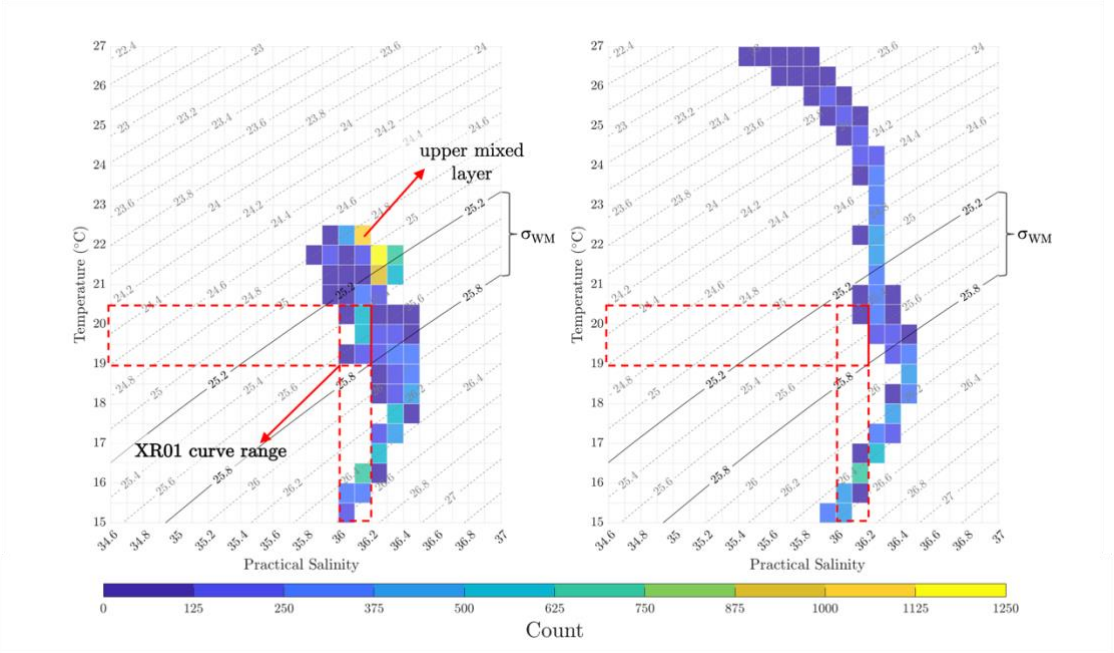

Fig. 3.7. Volumetric calculation of TS_P properties of the interpolated XR01 and XR02 transects (Fig. 3.1 and Fig. 3.2). 1 count unit corresponds to 111,000m^3. The intersection of the dashed red boxes is the hydrographic range of the XR01 curve that deviates from climatology in TS space (Fig 3.5 and Fig. 3.6). The density range of the water mass (25.2 kg/m^3 $\leq \sigma_{WM} \leq$ 25.8kg/m^3) is highlighted.

Table 3.1. Volumetric calculation of the dense water mass during XR01 and XR02.

Dataset	Count (bins)	Water mass % of cross-section within $25.2\ kg/m^3 \leq \sigma_{WM} \leq 25.8 kg/m^3$
XR01	4434	33.89
XR02	1369	10.46

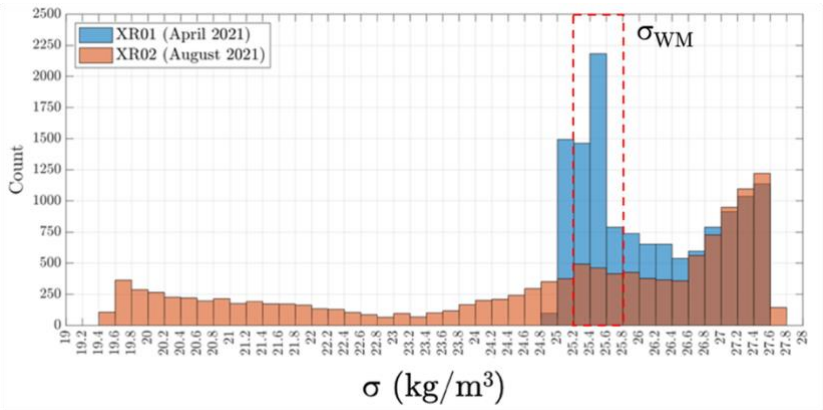

Fig. 3.8. Histogram (bins of $0.2 kg/m^3$) of density minus 1000 σ along the GL during XR01 and XR02. 1 count corresponds to $111{,}000 m^3$. The water mass density range ($25.2\ kg/m^3 \leq \sigma_{WM} \leq 25.8 kg/m^3$) is contained within the dashed red box.

3.1.4. Progressive vector diagrams (PVDs)

The PVDs at the TABS Buoys B, D, and X (Fig. 3.9) show the hourly current direction, SSS_P, and SST at each buoy for the timeframe 10 (t_0) – 16 (t_{end}) February 2021. This timeframe coincides with the observed salinity increase at Buoy B under the influence of the winter storms (Fig. 1.1).

At Buoys B and D, surface current direction is generally downcoast (southwestward), which is consistent with the Cochrane-Kelly scheme for non-summer months (Cochrane & Kelly, 1986). At the offshore Buoy X, which is located offshore of the 200m isobath, surface current direction is counterclockwise but also eventually progresses downcoast.

SST and SSS_P variability at Buoy X are relatively minimal: salinity values are relatively constant within the 36.1 – 36.2 range and temperature decreases from the 22°C – 22.5°C range to

~21°C. SSS_P at Buoy D increases to ~31.3 by 12 February 2021, becomes fresher at ~29 and remains within the range 29 – 30. Concurrently, SSS_P at Buoy B increases to a maximum of ~33 from around ~27.5. SST was cooler at Buoys B and D and decreased within the PVD timeframe. Buoy B SST cooled from ~15°C to ~13°C, and Buoy D from ~16°C to ~12°C. This variability in temperature during the winter storm event is most likely observed in Buoys B and D and not X due to their proximity to the coast, where cold air from the continent can influence SST.

The PVD interpretation is consistent with advection being the probable major influence in the recorded salinity increase at Buoy B during the winter storm event. While evaporation may have been a contributing variable, the PVDs indicate that the salinity increase was likely due to the advection of high-salinity water from offshore and/or upcoast (east/northeast). Current directions at Buoys D and X show that the high-salinity water at Buoy B likely did not come from downcoast (southwest).

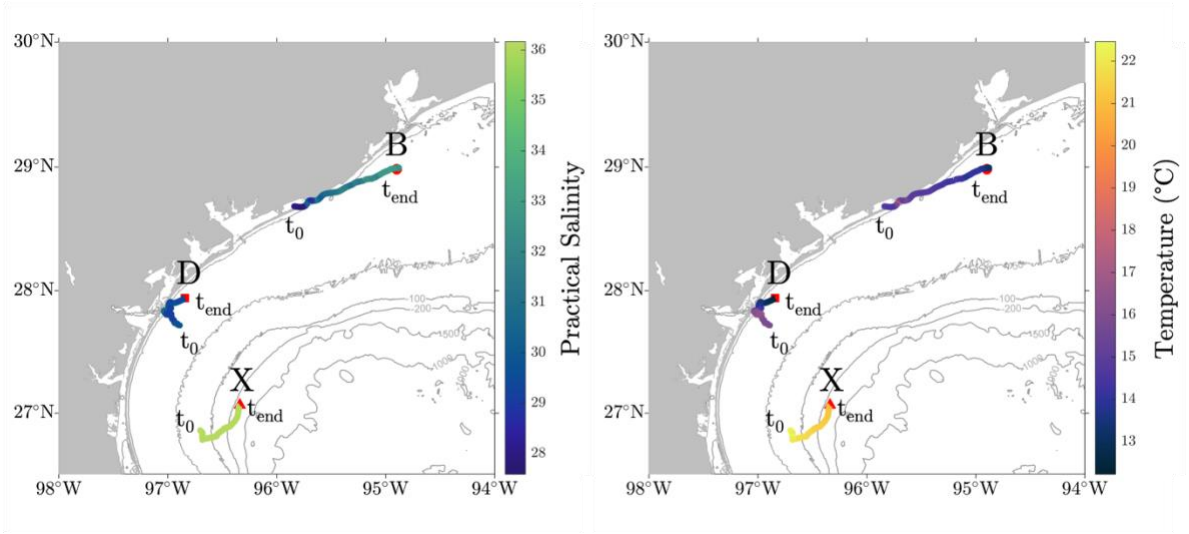

Fig. 3.9. Hourly Progressive vector diagrams (PVD) of SSS_P (left) and SST (right) of TABS Buoys B, D, and X from 10 (t_0) – 16 February (t_{end}) 2021.

3.2. General circulation model (GCM) results

3.2.1. Comparison of GCM and nearshore TABS network timeseries

In this section, TABS temperature and practical salinity data that are collected at 1.5m subsurface are assumed to be representative of surface data, and are compared with surface output (i.e., top-layer) from the GCM.

In the absence of freshwater input, the model captures the trend of coastal surface cooling during the winter outbreak, from 10-20 February 2021 (Fig. 3.10). TABS recorded a minimum temperature of 10.73°C on 21 Feb 2021, and the model reported a minimum temperature of 12.06°C on 19 Feb 2021. It can thus be said that coastal cooling during the formation of the dense water mass was caused largely by atmospheric forcing.

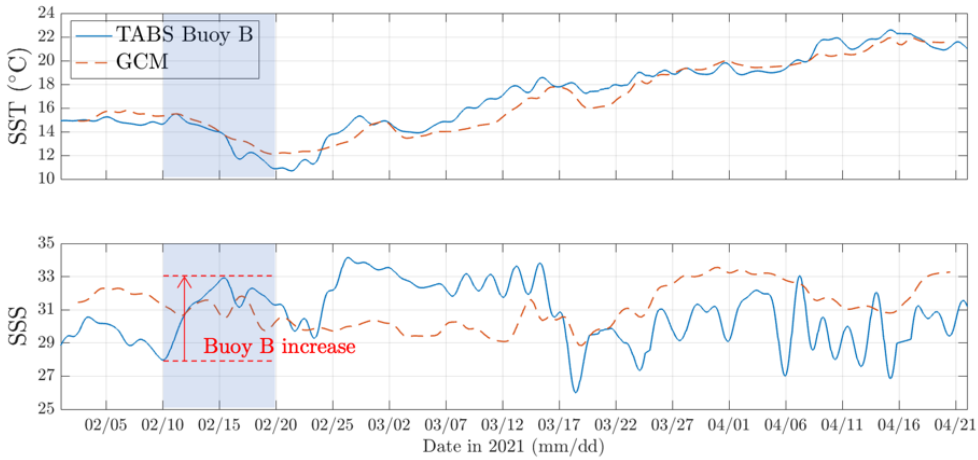

Fig. 3.10. Timeseries of sea surface temperature (SST, top) and sea surface salinity (SSS, bottom) from the TABS Buoy B (solid blue line) and from the GCM (dashed orange line) from February-April 2021. The duration of the winter storms (10-20 February) is within the shaded blue region where the Buoy B SSS_P increase occurs (red arrow).

Observed sea surface practical salinity (SSS_P) variations are not captured by the model. Even without freshwater input, the model's SSS_P values are lower than those recorded by TABS: TABS recorded a SSS_P increase by 5 from the beginning of the storm to around 5 days after

while under the influence of the storm. It is not known if this was solely due to evaporation: during a 1966 cold-air outbreak where dense water formed at the surface, a salinity increase of 1 was attributed to evaporation (Nowlin & Parker, 1974) (Fig. 3.11). The investigation into these scenarios exceeds the model's capability. The potential origin of the high-salinity surface water has been explored in Section 3.1.4; this water was likely advected from upcoast (east/northeast) .

3.2.2. Generation of dense surface water in the GCM

In Fig. 3.11, the temporal evolution of temperature and salinity along the GL from the GCM output before (8 Feb 2021) and during (16 Feb 2021) the winter event is seen, along with a modified figure from Nowlin and Parker showing the same variables before and during a cold-air outbreak in 1966 (1974). In both figures, triangles correspond to profiles at specific stations before the winter storm or cold-air outbreak, and circles correspond to the same stations during the storm. For the 2021 profiles, the stations are 2, 3, 4, 5, and 7; for the 1966 profiles, the stations are 13, 14, and 15.

In the 2021 diagram, the stations 2, 3, and 4 where significant water-column modification occurred are labeled on the plot and arrows point to the evolution of hydrographic properties at these stations in TS space from before to during the storm, at which point they are labeled 2', 3', and 4'. Triangular points enclosed in squares are representative of the surface mixed layer at each station before the storm, and circular points enclosed in circles correspond to the surface mixed layer during the storm. Similarly for the 1966 diagram, arrows point towards the evolution of hydrographic properties at Stations 13, 14, and 15 and are labeled as 13', 14', and 15' to correspond to the profiles during the cold-air outbreak.

In 2021 before the storm, stations 2 and 4 were represented by multiple points in TS space. During the storm, the same stations were represented by single points in TS space (2', 4')

– this indicates vertical mixing under the influence of the storm such that temperature and salinity are homogenous in the entire water-column at each station. The water-column in Station 3 was already well-mixed prior to the storm.

At Stations 2, 3, and 4, the entire water-column became denser during the storm, as indicated by rightward (salinity increase) and/or downward (temperature decrease) components of the arrows. At Station 3, both temperature and salinity contributed to the increase in water-column density. At Station 4, salinity was the main contributor, increasing by around 1 (from ~35 before the storm to ~36 during the storm). At the nearshore Station 2, however, cooling resulted in the density increase despite the water-column becoming fresher. This was not observed at TABS Buoy B (Fig. 3.6) where salinity increased during the winter storm event.

At the offshore stations deeper than the 100m isobath (Stations 5 and 7), density changes before and after the storm were relatively smaller in magnitude than the other stations: surface salinity at station 5 increased by 0.1 and station 7 decreased by 0.1.

In the 1966 diagram, significant modification due to the cold-air outbreak at Station 13 resulted in a salinity increase of ~+2 and a temperature decrease of ~1°C. Hydrographic properties of Station 13' are similar to those offshore and deeper in the water-column, where water of densities $26kg/m^3$ – $27kg/m^3$ typically reside. This corresponds to coastal dense water mass formation during the January 1966 cold-air outbreak.

Therefore, the GCM was able to simulate surface dense water properties due to atmospheric forcing – cooling and vertical mixing – although water-column modification in the model output, especially for salinities, was not as extensive as what was reported by Nowlin and Parker (1974).

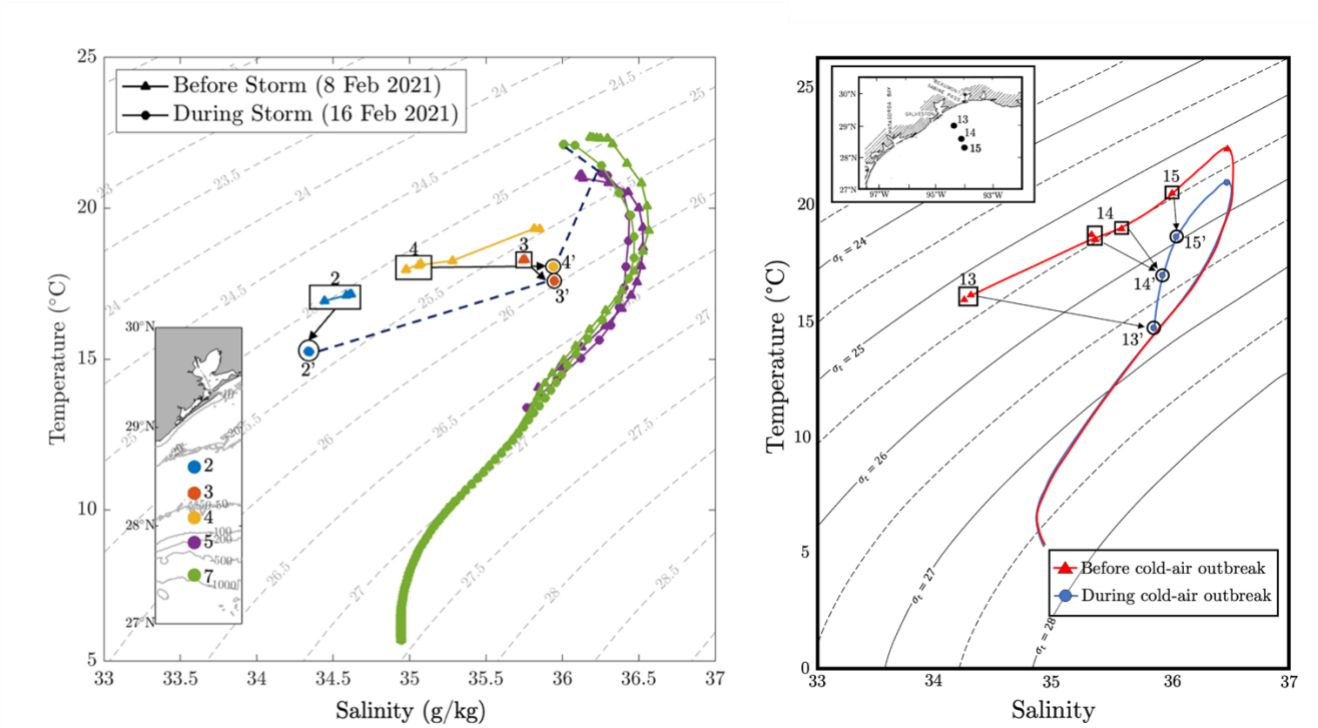

Fig. 3.11. **Left:** Temperature-Salinity diagram of GCM results of five stations along the GL (inset). Triangular points represent hydrographic data at each station (indicated by the different colors in the inset) before the winter storm event (8 Feb 2021), and circular points represent hydrographic data at the same depths at each station under the influence of the event (16 Feb 2021). The points corresponding to each station are separated by 10 m, starting from the surface (i.e., 0 m). Following from Nowlin and Parker (1974), triangular points enclosed in black squares and circular points enclosed in black circles represent the surface mixed layer at each indicated station before and during the event, respectively. Arrows indicate the temporal evolution of the mixed layer hydrographic properties in TS space, pointing from the station properties before the event (e.g. 2) to during the event (e.g. 2'). The dashed line connects the hydrographic properties at the surface of all stations during the storm. **Right:** Reprinted and modified from Nowlin and Parker (1974) during a cold-air outbreak in January 1966.

3.3. Idealized diffusion model results

Smoothed cross-sections from the idealized diffusion model are presented for the first timestep t_0 = 0 hours (Fig. 3.12), after t_{12} = 12 hours (Fig. 3.13), and the final timestep t_{336} = 336 hours = 2 weeks (Fig. 3.14). For the selected hydrographic parameter ranges (i.e., temperature T, practical salinity S_P, and density σ) used in these figures, the ranges across latitudes for these timesteps are in Table 3.2.

Table 3.2. Temperature (T), practical salinity (S_P), and density (σ) ranges for the idealized diffusion model timesteps t_0, t_{12}, and t_{336}. The lower and upper bounds of these ranges are determined by the colorbar limits in Fig. 3.12 to Fig. 3.14.

Timestep	Temperature (T) [°C]	Practical salinity (S_P)	Density minus 1000 (σ) [kg/m^3]
t_0 = 0 hours	$11°C \leq T_{t_0} \leq 24°C$	$35.4 \leq S_{P,t_0} \leq 36.6$	$25kg/m^3 \leq \sigma_{t_0} \leq 27kg/m^3$
t_{12} = 12 hours	$12.5°C \leq T_{t_{12}} \leq 23°C$	$35.6 \leq S_{P,t_{12}} \leq 36.6$	$25kg/m^3 \leq \sigma_{t_{12}} \leq 27kg/m^3$
t_{336} = 336 hours = 2 weeks	$12.9°C \leq T_{t_{336}} \leq 23°C$	$35.8 \leq S_{P,t_{336}} \leq 36.6$	$25kg/m^3 \leq \sigma_{t_{336}} \leq 27kg/m^3$

From t_0 to t_{336}, the T range narrowed with the lower bound increasing by 1.9°C and the upper bound decreasing by ~1°C, the S_P range narrowed with the lower bound increasing by ~0.4 and the upper bound remaining relatively constant, and the σ range remained relatively constant.

Due to the simulated cold temperatures, there is a high-density water mass (≥26kg/m^3) along the shelf at t_0 that extends past the shelf break at ~28.1°latitude (Fig. 3.12). In each cross-section, the 26kg/m^3 isopycnals from previous timesteps are also included to show the spatiotemporal evolution of this water mass. Because the convective adjustment increases the vertical diffusivity κ_V by 10 when denser water is above lighter water, the water mass quickly

sinks to its density compensation depth within 50 – 100m and mixes along its isopycnal so that by t_{12}, the water mass no longer extends to the open ocean (Fig. 3.13). By t_{336}, much of the high-density water that was initially on the shelf had moved to the open ocean; the 26kg/m^3 isopycnal had increased in volume and sank and mixed with water of the same density deeper in the water-column (Fig. 3.14). The larger changes to the temperature range from t_0 to t_{336} and visual assessment of the temperature and salinity contours of all cross-sections show density differences in this model are driven by temperature variation.

Differences in the cross-sections (Fig. 3.15) show the spatiotemporal evolution of the 26kg/m^3 high-density water mass during the model run. The upper water-column (< 30m) along the shelf became saltier ($0 \leq \Delta S_P \leq +0.8$), and the full water-column up to 28.2°latitude became warmer ($0°C \leq \Delta T \leq +2°C$) and less dense ($-0.5kg/m^3 \leq \Delta\sigma \leq 0kg/m^3$). However, along the outer shelf at depths <50m, the water became significantly colder and denser, ΔT up to -4°C and $\Delta\sigma$ up to +1kg/m^3. Practical salinity changes offshore are relatively minimal ($\Delta S_P = \pm 0.2$), but at depths <100m, the water-column became colder and denser, with ΔT up to -2°C and $\Delta\sigma$ up to +0.5kg/m^3. This is due to the offshore movement of the high-density water mass along the shelf and diapycnal mixing between the water mass and ambient water in the upper water-column of the open ocean.

In the model, dense water along the shelf cascaded and moved seaward and sank to its density compensation depth. Therefore, under only the influence diffusion and gravity (via convective adjustment) and without any external variation to the hydrography of the model, the idealized diffusion model can simulate basic processes of cascading, i.e., diapycnally mixing with ambient water and sinking. When the water mass is along the shelf, it can only undergo

diapycnal mixing because water with the same density is found offshore and at depth (~100m); this mixing resulted in the increase in volume of the 26kg/m^3 isopycnal along the outer shelf.

Observed isopycnal convergence during cascading in the XR01 cross-sections (Fig. 3.1) does not occur in the model. A major contributing factor to this absence is the limited dimensionality in the idealized diffusion model that only allows for zonal (across latitudes) and vertical (across depths) mixing. Without meridional spreading or external input to enhance diapycnal mixing, the isopycnals cannot converge without violating this conservation of mass.

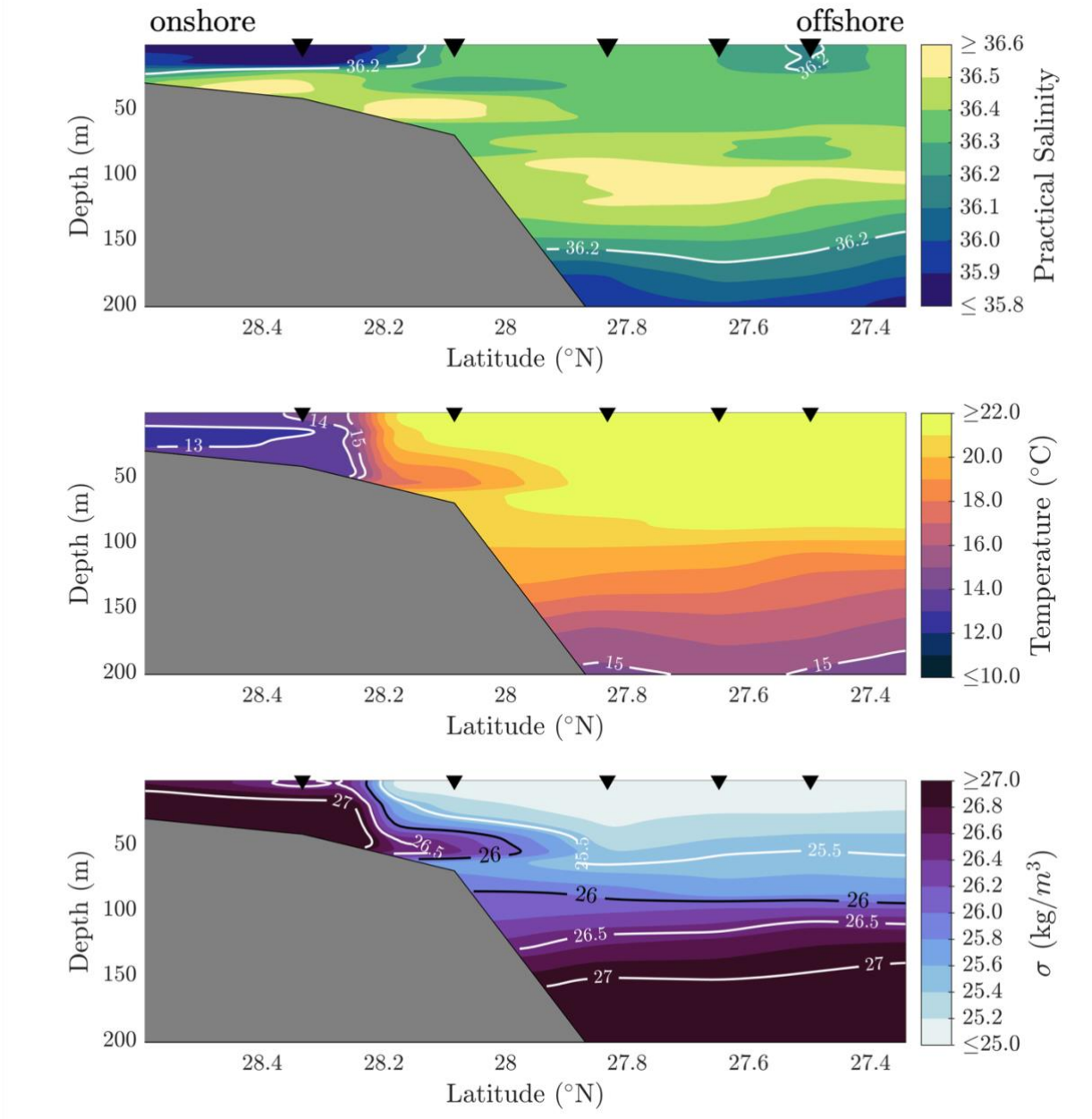

Fig. 3.12. Smoothed practical salinity (top), temperature (middle), and density minus 1000 (σ) (bottom) of the idealized diffusion model at $t_0 = 0$ hours. Black triangles are XR05 data collection latitudes. The 26kg/m^3 isopycnals, i.e., the high-density water mass along the shelf and in the offshore deep ocean, are highlighted.

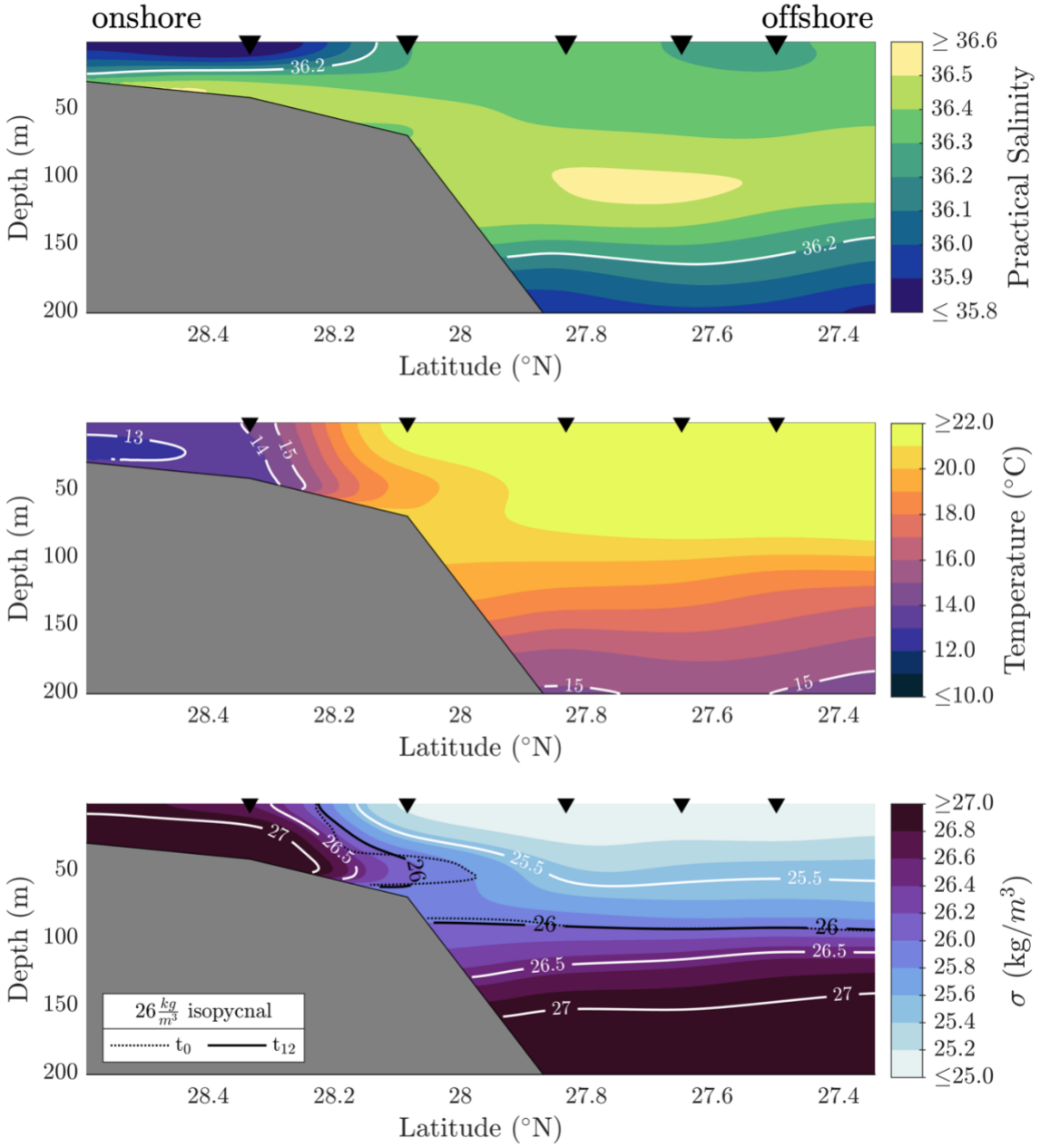

Fig. 3.13. Smoothed practical salinity (top), temperature (middle), and density minus 1000 (σ) (bottom) of the idealized diffusion model at t_{12} = 12 hours. Black triangles are XR05 data collection latitudes. The current timestep 26kg/m^3 isopycnals, and those for t_0 are also shown.

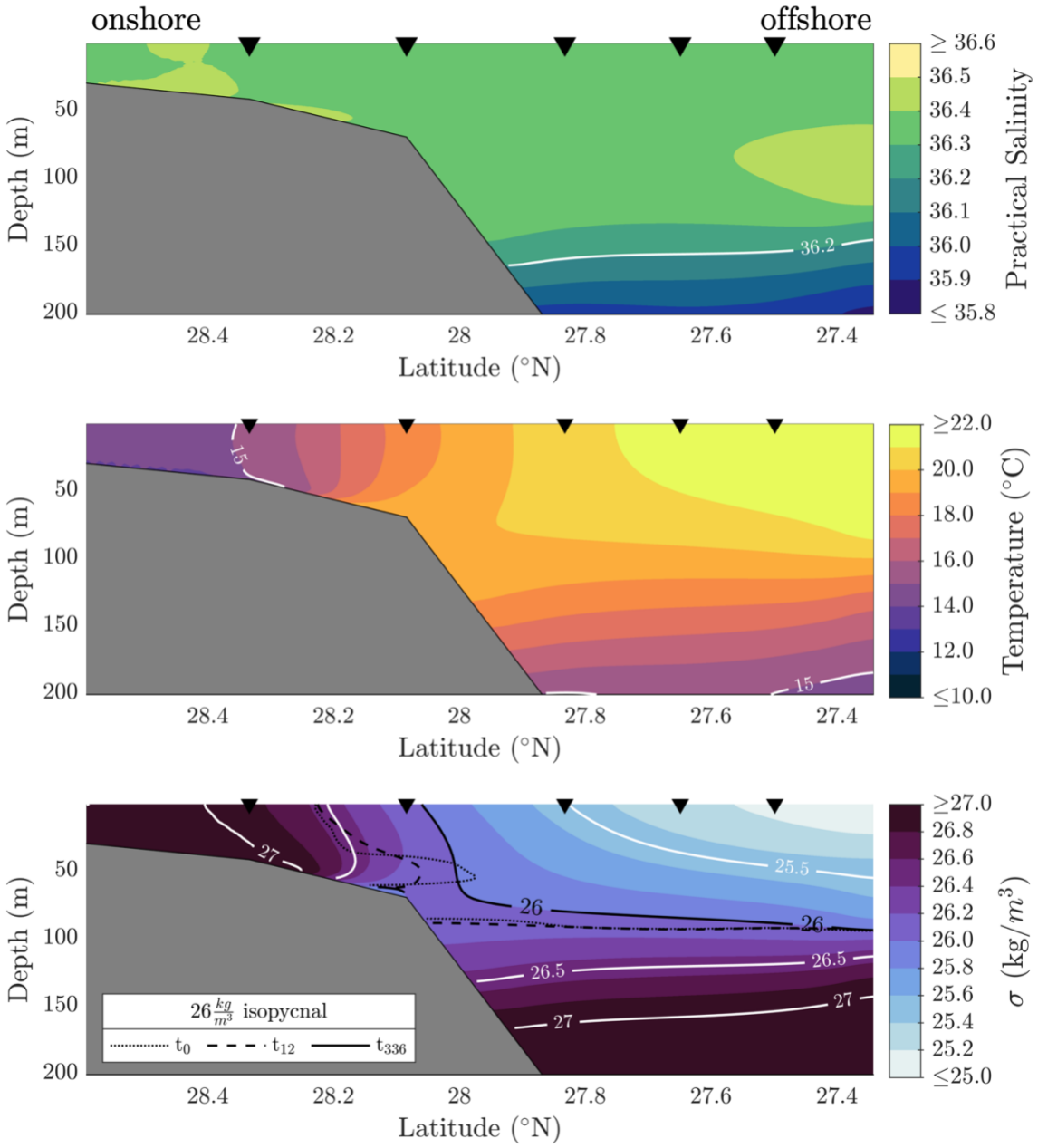

Fig. 3.14. Smoothed practical salinity (top), temperature (middle), and density minus 1000 (σ) (bottom) of the idealized diffusion model at t_{336} = 336 hours = 2 weeks. Black triangles are XR05 data collection latitudes. The current timestep 26kg/m^3 isopycnals, and those for t_0 and t_{12} are also shown.

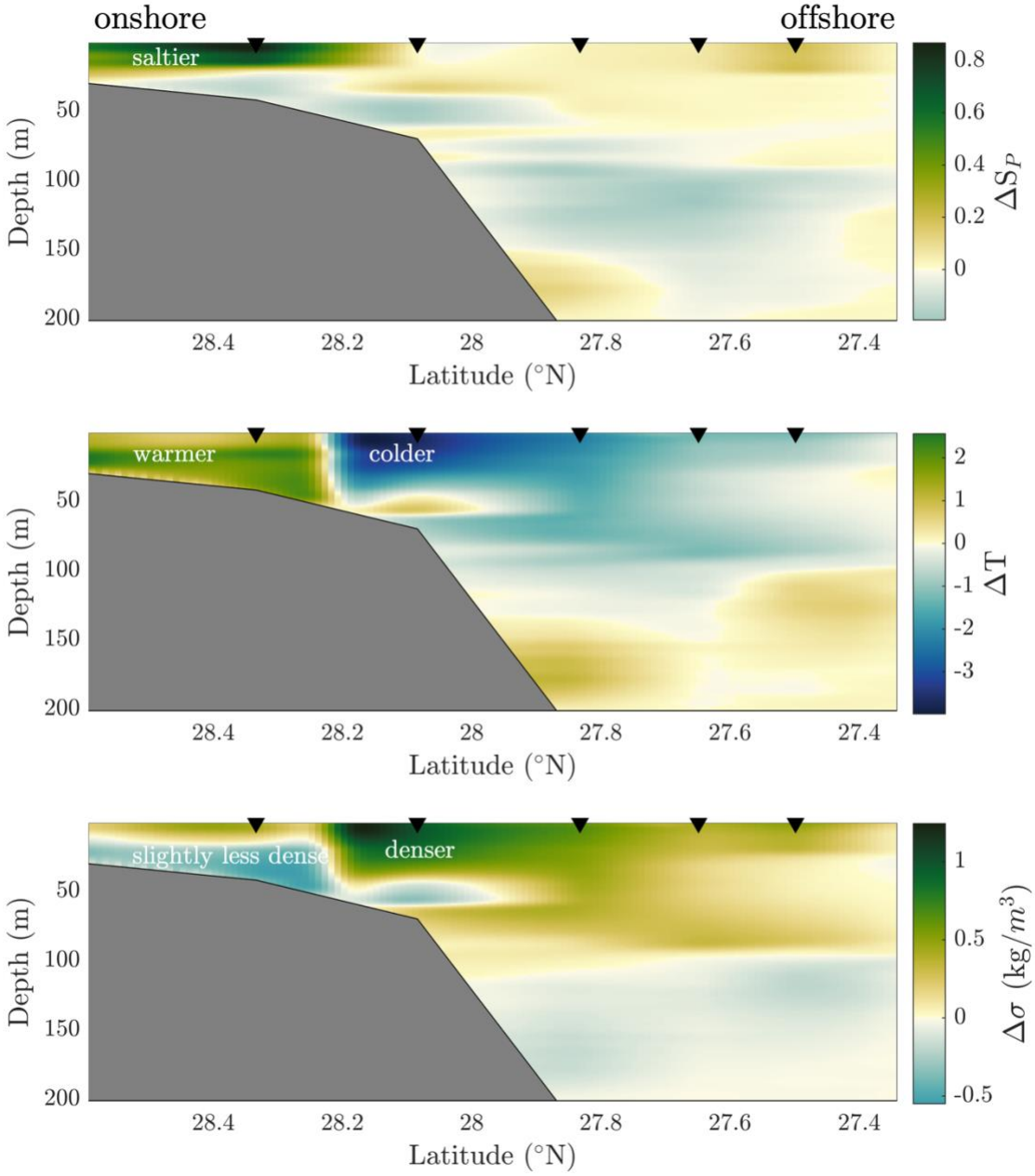

Fig. 3.15. Differences (Δ) between the final (t_{336}, Fig. 3.14) and first (t_0, Fig. 3.12) timesteps of the idealized diffusion model of smoothed practical salinity (S_P) (top), temperature (T) (middle), and density minus 1000 (σ) (bottom). Black triangles are XR05 data collection latitudes. Text annotations (saltier, warmer, etc.) refer to conditions of t_{336} in comparison to those at t_0.

4. SUMMARY AND CONCLUSIONS

Decades of observational data and high-resolution numerical output in the northwestern Gulf of Mexico were used to investigate the formation and fate of a coastal dense water mass during the February 2021 Texas winter storms. Two hypotheses were tested in this study: hypothesis **H1**: Strong northeasterly winds during the February 2021 winter storms caused negative heat exchange (heat loss), increased evaporation, and mixing, resulting in the formation of a surface dense water mass in the coastal northwestern Gulf of Mexico, and hypothesis **H2**: The surface dense water mass that formed during the February 2021 winter storms mixed with ambient seawater, moved offshore past the shelf break, and dissipated by late summer 2021.

In February 2021, the coastal Texas A&M Buoy System (TABS) network near Galveston Bay measured record-low surface temperatures (a minimum of 10.73°C) in response to below-freezing air temperatures (as low as -8.64°C) during severe winter storms. Surface practical salinity values increased by ~5 within this timeframe. Days after this event, surface densities at the buoy reached 1025.25 kg/m^3, an unusual value for this coastal region.

A series of research cruises that collected hydrographic profiles south of Galveston Bay from the continental shelf to offshore along 95°W months after the winter storms found that water-column densities along the repeat transects were consistent with the measured surface densities during the event and were present in quantity and in locations in the water-column where they are not typically found. This density anomaly manifested in April 2021 as a subductive tongue, i.e., a distinct water mass characterized by an isohaline of 36.2 that extended from the shelf (≥~28°latitude and depths above 60m) to offshore (in between in between ~27.5° – 27.8°latitude at depths ~30m – 60m) and whose density range lower bound (25.2kg/m^3 –

25.8kg/m^3) corresponded to the surface densities during the event, revealing the zonal and vertical spatial scale of the event. The isopycnals within the volume of the tongue were converging from the full water-column along the shelf to neutral depth beneath the 22°C upper mixed layer. Due to conservation of mass, the convergence pointed to offshore movement of the water mass and potential lateral or meridional spreading under the mixed layer, supporting **H2**. Furthermore, the temperature and salinity profiles along the transect showed that the signal of the tongue weakened from April to September 2021, revealing the temporal scale of the event. Comparison between 2021 profiles with climatology from 1995-2023 further substantiated that the tongue was anomalous and mixed with ambient water as it cascaded, also supporting **H2**.

Surface measurements from the TABS network were compared with numerical output and showed that atmospheric forcing (heat loss) was the likely main driver behind the cooling of SST, supporting the negative heat exchange in hypothesis **H1**. Representation of the same numerical output in TS space showed the formation of a coastal dense water mass and homogenous water-columns along the GL during the winter storms, substantiating the vertical mixing aspect of hypothesis **H1**. Although simulating modifications to surface salinities exceeded the model's capabilities, PVDs showing downcoast surface current directions at three buoys in the northwestern Gulf of Mexico from the TABS network point to advection of high-salinity water from upcoast or offshore as the likely source of surface salinity increases recorded by TABS during the event.

Finally, a two-dimensional idealized diffusion model initialized with ocean conditions that simulated the hydrographic modifications made by the 2021 winter storms was able to account for basic features of water mass cascading: a dense plume along the continental shelf was able to spread zonally (across latitudes) and vertically (across depths) and sink to neutral

depth using only diffusion/diapycnal mixing and gravity. However, the model did not recreate some processes that were observed in the hydrographic data such as the convergence of isopycnals. Furthermore, other processes such as tides, advection, atmospheric forcing, etc. would need to be added for a more accurate simulation.

The methods used in this study may be applied to other instances of observed anomalous hydrographic properties to investigate the formation and fate of coastal water masses. To build upon this study, future work could investigate the meridional extent of the water mass using remote sensing and satellite data and consider residence times or even inertial frequencies to explain the water mass's months-long occupancy along the continental shelf. Improvements to both the general circulation model and the idealized diffusion model should be made to accurately represent the atmospheric and oceanic conditions during the winter storm event and to realistically simulate the processes that modified the hydrographic properties of the shelf waters and the water mass. Finally, this work may be expanded upon by assessing the ecological impact that these water masses may have under future climate scenarios and/or more frequent cold air outbreaks.

REFERENCES

Barbero, L., Pierrot, D., Wanninkhof, R., Baringer, M. O., Byrne, R. H., Langdon, C., Zhang, J.-Z., & Stauffer, B. A. (2019). *Dissolved inorganic carbon, total alkalinity, nutrients, and other variables collected from CTD profile, discrete bottle, and surface underway observations using CTD, Niskin bottle, flow-through pump, and other instruments from NOAA Ship Ronald H. Brown in the Gulf of Mexico, Southeastern coast of the United States, and Mexican and Cuban coasts during the third Gulf of Mexico and East Coast Carbon (GOMECC-3) Cruise from 2017-07-18 to 2017-08-20 (NCEI Accession 0188978)*. NOAA National Centers for Environmental Information. https://doi.org/10.25921/yy5k-dw60

Bernardi Aubry, F., Falcieri, F. M., Chiggiato, J., Boldrin, A., Luna, G. M., Finotto, S., Camatti, E., Acri, F., Sclavo, M., & Carniel, S. (2018). Massive shelf dense water flow influences plankton community structure and particle transport over long distance. *Scientific Reports*, *8*(1), 4554.

Burnett, J. (2021, March 13). *Texas "cold-stun" of 2021 was largest sea turtle rescue in history, scientists say*. NPR. https://www.npr.org/2021/03/13/976105783/texas-cold-stun-of-2021-was-largest-sea-turtle-rescue-in-history-scientists-say

Canals, M., Puig, P., de Madron, X. D., Heussner, S., Palanques, A., & Fabres, J. (2006). Flushing submarine canyons. *Nature*, *444*(7117), 354–357.

Cervantes-Díaz, G. Y., Hernández-Ayón, J. M., Zirino, A., Herzka, S. Z., Camacho-Ibar, V., Norzagaray, O., Barbero, L., Montes, I., Sudre, J., & Delgado, J. A. (2022). Understanding upper water mass dynamics in the Gulf of Mexico by linking physical and biogeochemical features. *Journal of Marine Systems*, *225*, 103647. https://doi.org/10.1016/j.jmarsys.2021.103647

Cochrane, J. D., & Kelly, F. J. (1986). Low-frequency circulation on the Texas-Louisiana continental shelf. *Journal of Geophysical Research*, *91*(C9), 10645. https://doi.org/10.1029/JC091iC09p10645

Dagg, M. J. (1988). Physical and biological responses to the passage of a winter storm in the coastal and inner shelf waters of the northern Gulf of Mexico. *Continental Shelf Research*, *8*(2), 167–178. https://doi.org/10.1016/0278-4343(88)90052-0

DiMarco, S. F., Jochens, A. E., & Howard, M. K. (1997). *LATEX Shelf Data Report: Current Meter Moorings, April 1992 to December 1994*.

DiMarco, S. F., Nowlin, W. D., & Reid, R. O. (2005). A statistical description of the velocity fields from upper ocean drifters in the Gulf of Mexico. *Geophysical Monograph-American Geophysical Union*, *161*, 101.

DiMarco, S. F., Strauss, J., May, N., Mullins-Perry, R. L., Grossman, E. L., & Shormann, D. (2012). Texas Coastal Hypoxia Linked to Brazos River Discharge as Revealed by Oxygen Isotopes. *Aquatic Geochemistry*, *18*(2), 159–181. https://doi.org/10.1007/s10498-011-9156-x

Doss-Gollin, J., Farnham, D. J., Lall, U., & Modi, V. (2021). How unprecedented was the February 2021 Texas cold snap? *Environmental Research Letters*, *16*(6), 064056.

Fernández-Nóvoa, D., Costoya, X., Kobashi, D., Rodríguez-Díaz, L., deCastro, M., & Gómez-Gesteira, M. (2020). Influence of Mississippi and Atchafalaya River plume in the winter coastal cooling of the Northwestern Gulf of Mexico. *Journal of Marine Systems*, *209*, 103374. https://doi.org/10.1016/j.jmarsys.2020.103374

Finch, R. H. (1917). Fish killed by the cold wave of February 2–4, 1917, in Florida. *Monthly Weather Review*, *45*(4), 171–172.

Fu, D., Small, J., Kurian, J., Liu, Y., Kauffman, B., Gopal, A., Ramachandran, S., Shang, Z., Chang, P., & Danabasoglu, G. (2021). Introducing the New Regional Community Earth System Model, R-CESM. *Bulletin of the American Meteorological Society*, *102*(9), E1821–E1843.

Gunter, G. (1941). Death of fishes due to cold on the Texas coast, January, 1940. *Ecology*, *22*(2), 203–208.

Gunter, G. (1951). Destruction of fishes and other organisms on the south Texas coast by the cold wave of January 28-February 3, 1951. *Ecology*, *32*(4), 731–736.

Hamilton, P., Leben, R., Bower, A., Furey, H., & Pérez-Brunius, P. (2018). Hydrography of the Gulf of Mexico Using Autonomous Floats. *Journal of Physical Oceanography*, *48*(4), 773–794. https://doi.org/10.1175/JPO-D-17-0205.1

Hickey, B. M., MacCready, P., Elliott, E., & Kachel, N. B. (2000). Dense saline plumes in Exuma Sound, Bahamas. *Journal of Geophysical Research: Oceans*, *105*(C5), 11471–11488. https://doi.org/10.1029/2000JC900004

Intergovernmental Oceanographic Commission. (2015). *The International thermodynamic equation of seawater–2010: Calculation and use of thermodynamic properties.[includes corrections up to 31st October 2015]*.

Ivanov, V. V., Shapiro, G. I., Huthnance, J. M., Aleynik, D. L., & Golovin, P. N. (2004). Cascades of dense water around the world ocean. *Progress in Oceanography*, *60*(1), 47–98. https://doi.org/10.1016/j.pocean.2003.12.002

JRA-55: Japanese 55-year Reanalysis, Daily 3-Hourly and 6-Hourly Data. (2013). Research Data Archive at the National Center for Atmospheric Research, Computational and Information Systems Laboratory. https://doi.org/10.5065/D6HH6H41

Kemp, D. W., Oakley, C. A., Thornhill, D. J., Newcomb, L. A., Schmidt, G. W., & Fitt, W. K. (2011). Catastrophic mortality on inshore coral reefs of the Florida Keys due to severe low-temperature stress. *Global Change Biology*, *17*(11), 3468–3477.

Langdon, C., & Rosenstiel School of Marine and Atmospheric Science. (2011). *Temperature, salinity, nutrients, freons, oxygen, currents (ADCP), underway and other measurements collected in the Gulf of Mexico and Atlantic as part of the Gulf of Mexico and East Coast Carbon Cruise (GOMECC) 2007 (NCEI Accession 0066603)*. NOAA National Centers for Environmental Information. https://accession.nodc.noaa.gov/0066603

Lellouche, J.-M., Greiner, E., Le Galloudec, O., Garric, G., Regnier, C., Drevillon, M., Benkiran, M., Testut, C.-E., Bourdalle-Badie, R., & Gasparin, F. (2018). Recent updates to the Copernicus Marine Service global ocean monitoring and forecasting real-time 1⁄12 high-resolution system. *Ocean Science*, *14*(5), 1093–1126.

Li, Y., Nowlin Jr, W. D., & Reid, R. O. (1996). Spatial-scale analysis of hydrographic data over the Texas-Louisiana continental shelf. *Journal of Geophysical Research: Oceans*, *101*(C9), 20595–20605.

MATLAB version: 9.13.0 (R2022b). (2023). The MathWorks Inc. https://mathworks.com

McDougall, T. J., & Barker, P. M. (2011). Getting started with TEOS-10 and the Gibbs Seawater (GSW) oceanographic toolbox. *Scor/Iapso WG*, *127*(532), 1–28.

Morrison, J. M., Merrell, W. J., Key, R. M., & Key, T. C. (1983). Property distributions and deep chemical measurements within the western Gulf of Mexico. *Journal of Geophysical Research*, *88*(C4), 2601. https://doi.org/10.1029/JC088iC04p02601

Nowlin, W. D., Jochens, A. E., DiMarco, S. F., Reid, R. O., & Howard, M. K. (2005). Low-frequency circulation over the Texas-Louisiana continental shelf. *Geophysical Monograph-American Geophysical Union*, *161*, 219.

Nowlin, W. D., Jochens, A. E., Reid, R. O., & DiMarco, S. F. (1998a). *Texas-Louisiana Shelf Circulation and Transport Processes Study: Synthesis Report, Volume 1. Technical Report*.

Nowlin, W. D., Jochens, A. E., Reid, R. O., & DiMarco, S. F. (1998b). *Texas-Louisiana Shelf Circulation and Transport Processes Study: Synthesis Report, Volume 2. Appendices*.

Nowlin, W., & Parker, C. A. (1974). Effects of a cold-air outbreak on shelf waters of the Gulf of Mexico. *Journal of Physical Oceanography*, *4*(3), 467–486.

Passalacqua, G. A., Sheinbaum, J., & Martinez, J. A. (2016). Sea surface temperature influence on a winter cold front position and propagation: Air–sea interactions of the 'Nortes' winds in the Gulf of Mexico. *Atmospheric Science Letters*, *17*(5), 302–307. https://doi.org/10.1002/asl.655

Pawlowicz, R. (2020). M_Map: A mapping package for Matlab. *Computer Software*.

Portela, E., Tenreiro, M., Pallàs-Sanz, E., Meunier, T., Ruiz-Angulo, A., Sosa-Gutiérrez, R., & Cusí, S. (2018). Hydrography of the central and western Gulf of Mexico. *Journal of Geophysical Research: Oceans*, *123*(8), 5134–5149.

Porter, J. W., Battey, J. F., & Smith, G. J. (1982). Perturbation and change in coral reef communities. *Proceedings of the National Academy of Sciences*, *79*(5), 1678–1681.

Redi, M. H. (1982). Oceanic isopycnal mixing by coordinate rotation. *Journal of Physical Oceanography*, *12*(10), 1154–1158.

Roberts, H. H., Rouse, Jr., L. J., Walker, N. D., & Hudson, J. H. (1982). Cold-water Stress in Florida Bay and Northern Bahamas: A Product of Winter Cold-Air Outbreaks. *SEPM Journal of Sedimentary Research, Vol. 52*. https://doi.org/10.1306/212F7EFA-2B24-11D7-8648000102C1865D

Shapiro, G. I. (2003). Dense water cascading off the continental shelf. *Journal of Geophysical Research*, *108*(C12), 3390. https://doi.org/10.1029/2002JC001610

Shapiro, G. I., & Hill, A. E. (1997). Dynamics of Dense Water Cascades at the Shelf Edge. *Journal of Physical Oceanography*, *27*(11), 2381–2394. https://doi.org/10.1175/1520-0485(1997)027<2381:DODWCA>2.0.CO;2

Thomson, R. E., & Emery, W. J. (2014). *Data analysis methods in physical oceanography*. Newnes.

Thyng, K. M., Greene, C. A., Hetland, R. D., Zimmerle, H. M., & DiMarco, S. F. (2016). True colors of oceanography: Guidelines for effective and accurate colormap selection. *Oceanography*, *29*(3), 9–13.

UNESCO, I. (1981). The practical salinity scale1978 and the international equation of state of seawater 1980. *Tenth Report of the Joint Panel on Oceanographic Tables and Standards (JPOTS)*, *25*.

Vilibić, I., & Šantić, D. (2008). Deep water ventilation traced by Synechococcus cyanobacteria. *Ocean Dynamics*, *58*, 119–125.

Walker, N. D., Roberts, H. H., Rouse, L. Jr., & Huh, O. K. (1982). Thermal history of reef-associated environments during a record cold-air outbreak event. *Coral Reefs*, *1*, 83–87.

Walker, N. D., Rouse, L. J., & Huh, O. K. (1987). Response of subtropical shallow-water environments to cold-air outbreak events: Satellite radiometry and heat flux modeling. *Continental Shelf Research*, *7*(7), 735–757. https://doi.org/10.1016/0278-4343(87)90014-8

Walpert, J. N., Knap, A. H., DiMarco, S. F., & Buschang, S. G. (2020). Texas Automated Buoy System (TABS): 25 Years Providing Data for Spill Response, Modeling and Research. *Global Oceans 2020: Singapore–US Gulf Coast*, 1–7.

Wanninkhof, R., Pierrot, D., & Sullivan, K. F. (2021). *Partial pressure of carbon dioxide, temperature, salinity and other variables collected from surface underway observations during NOAA Ship Ronald H. Brown cruises in the Caribbean Sea, Gulf of Mexico, North Pacific Ocean, Atlantic Ocean in 2021 (NCEI Accession 0228760).* [Data set]. NOAA National Centers for Environmental Information. https://doi.org/10.25921/0er3-0c38

Whitehead, J. (1993). A laboratory model of cooling over the continental shelf. *Journal of Physical Oceanography*, *23*(11), 2412–2427.

Wilkin, J. L., Bowen, M. M., & Emery, W. J. (2002). Mapping mesoscale currents by optimal interpolation of satellite radiometer and altimeter data. *Ocean Dynamics*, *52*, 95–103.

Wilson, P. A., & Roberts, H. H. (1995). Density cascading; off-shelf sediment transport, evidence and implications, Bahama Banks. *Journal of Sedimentary Research*, *65*(1a), 45–56.

Yoder, J. A., & Ishimaru, T. (1989). Phytoplankton advection off the southeastern United States continental shelf. *Continental Shelf Research*, *9*(6), 547–553.

Zhang, X., Hetland, R. D., Marta-Almeida, M., & DiMarco, S. F. (2012). A numerical investigation of the Mississippi and Atchafalaya freshwater transport, filling and flushing times on the Texas-Louisiana Shelf. *Journal of Geophysical Research: Oceans*, *117*(C11).